eprints@whiterose.ac.uk
https://eprints.whiterose.ac.uk/

Deep ALMA photometry of distant X-ray AGN: improvements in star formation rate constraints, and AGN identification

F. Stanley,[1,2]★ C. M. Harrison,[2,3] D. M. Alexander,[2] J. Simpson,[4] K. K. Knudsen,[1] J. R. Mullaney,[5] D. J. Rosario[2] and J. Scholtz[2]

[1]*Department of Space, Earth and Environment, Chalmers University of Technology, Onsala Space Observatory, SE-43992 Onsala, Sweden*
[2]*Centre for Extragalactic Astronomy, Department of Physics, Durham University, South Road, Durham DH1 3LE, UK*
[3]*European Southern Observatory, Karl-Schwarzschild-Str. 2, D-85748, Garching b. München, Germany*
[4]*Academia Sinica Institute of Astronomy and Astrophysics (ASIAA), No. 1, Section 4, Roosevelt Rd., Taipei 10617, Taiwan*
[5]*Department of Physics and Astronomy, University of Sheffield, Hounsfield Road, Sheffield S3 7RH, UK*

ABSTRACT

We present the star formation rates (SFRs) of a sample of 109 galaxies with X-ray-selected active galactic nuclei (AGNs) with moderate to high X-ray luminosities ($L_{2-8\,keV}$ = $10^{42} - 10^{45}$ erg s^{-1}), at redshifts $1 < z < 4.7$, that were selected to be faint or undetected in the *Herschel* bands. We combine our deep Atacama large (sub-)millimetre array (ALMA) continuum observations with deblended 8–500 µm photometry from *Spitzer* and *Herschel*, and use infrared (IR) spectral energy distribution (SED) fitting and AGN – star formation decomposition methods. The addition of the ALMA photometry results in an order of magnitude more X-ray AGN in our sample with a measured SFR (now 37 %). The remaining 63 % of the sources have SFR upper limits that are typically a factor of 2–10 times lower than the pre-ALMA constraints. With the improved constraints on the IR SEDs, we can now identify a mid-IR (MIR) AGN component in 50 % of our sample, compared to only ∼1 % previously. We further explore the $F_{870\,\mu m}/F_{24\,\mu m}$–redshift plane as a tool for the identification of MIR-emitting AGN, for three different samples representing AGN-dominated, star formation-dominated, and composite sources. We demonstrate that the $F_{870\,\mu m}/F_{24\,\mu m}$–redshift plane can successfully split between AGN and star formation-dominated sources, and can be used as an AGN identification method.

Key words: galaxies: active – galaxies: evolution – galaxies: star formation.

1 INTRODUCTION

The impact of the energetic output of a galaxy's active galactic nucleus (AGN) on the surrounding interstellar medium (ISM), and the galaxy's ongoing star formation, is one of the main open questions in the study of galaxy evolution (e.g. see Alexander & Hickox 2012; Fabian 2012; Harrison 2017, for reviews). Studies of the mean star formation rates (SFRs) of distant X-ray AGN, have repeatedly shown that, on average, AGN live in star-forming galaxies (e.g. Lutz et al. 2010; Shao et al. 2010; Mullaney et al. 2012b; Harrison et al. 2012; Rosario et al. 2012; Rosario et al. 2013; Azadi et al. 2015; Stanley et al. 2015). Furthermore, studies looking into the trends of the mean SFRs as a function of X-ray and/or bolometric AGN luminosity appear to be, after some discrepancy (e.g. Page et al. 2012; Rosario et al. 2012; Harrison et al. 2012), converging to the conclusion that there is a flat trend between the mean SFRs as a function

of AGN luminosity for X-ray-selected AGN (e.g. Azadi et al. 2015; Stanley et al. 2015; Lanzuisi et al. 2017). The flat trend has been interpreted as a result of the stochasticity of the AGN that has shorter time-scales than that of galaxy-wide SFR (e.g. Gabor & Bournaud 2013; Hickox et al. 2014; Volonteri et al. 2015; Stanley et al. 2015; Lanzuisi et al. 2017). Indeed, studies find a correlation when averaging the AGN luminosity as a function of the SFR (e.g. Rafferty et al. 2011; Mullaney et al. 2012a; Chen et al. 2013; Delvecchio et al. 2014). This can be interpreted as evidence for an underlying long-term correlation of AGN activity and star formation (although see McAlpine et al. 2017 for an alternative explanation).

Studies of luminous optical quasars have repeatedly found a positive trend between the mean SFRs as a function of bolometric AGN luminosity (e.g. Bonfield et al. 2011; Rosario et al. 2013; Kalfount-zou et al. 2014; Gürkan et al. 2015; Harris et al. 2016; Stanley et al. 2017). However, in our recent study of Stanley et al. (2017), we argue that the positive trend observed is not a result of AGN-driven enhancement, but it is driven by galaxy properties such as stellar mass (M_*) and redshift (z) (also see Yang et al. 2017).

★ E-mail: flora.stanley@chalmers.se

The above observational evidence may lead to the conclusion that AGN have no effect on the SFR of their host galaxies. However, AGN feedback (i.e. where the large energy outputs of the AGN cause heating and/or outflows of a galaxy's gas) is a necessary component of cosmological hydrodynamical simulations of galaxy evolution (e.g. Bower et al. 2006; Genel et al. 2014; Schaye et al. 2015). Recent work by McAlpine et al. (2017) that studied the galaxies that host AGN in the EAGLE (i.e. Evolution and Assembly of GaLaxies and their Environments; Schaye et al. 2015) simulation, that incorporates AGN feedback, successfully reproduces the observational results of a flat trend between the mean SFR as a function of AGN luminosity for AGN selected samples, as well as those of a correlation of the mean AGN luminosity as a function of SFR. The fact that a simulation incorporating AGN feedback can reproduce the above flat trends demonstrates that we cannot rule out that AGN have an impact on their host galaxies (Harrison 2017). It may be that the signatures of AGN feedback are much more subtle than what is able to be traced by looking at the mean properties of AGN samples. However, the limitations presented by studying means, can be overcome by placing strong constraints on the underlying distribution (e.g. Mullaney et al. 2015; Scholtz et al. 2018).

The main restriction in accurately measuring the distributions of SFRs of high-redshift ($z > 0.2$) AGN samples has been the limitations on the sensitivity of the available photometry. *Herschel* has provided the deepest field-survey observations in the far-infrared (FIR) at 70–500 µm, but even so the available surveys only detect the bright end of the galaxy population. For $z \gtrsim 1$, we can only detect star-bursting and/or massive star-forming galaxies. Consequently, in order to directly constrain the SFRs of the typical population of galaxies and AGN at redshifts of $z \gtrsim 1$, we need even deeper observations in the FIR/sub-millimetre (sub-mm). Today, the Atacama large (sub-)millimetre array (ALMA) can achieve that. With ALMA, it is now possible to easily detect and resolve galaxies at redshifts above $z \sim 1$ at lower fluxes than that possible with previous FIR/sub-mm observatories, and place more accurate constraints on the SFRs of fainter galaxies with and without AGN. This has been demonstrated previously in Mullaney et al. (2015), where it was shown that with ALMA photometry, it is possible to distinguish differences between the distribution of the SFRs of a sample of X-ray AGN, and that of the overall population of star-forming galaxies. Despite the limited number of targets in the study of Mullaney et al. (2015) (i.e. 24 X-ray AGN targets), the results highlight the importance of constraining the distribution of SFRs rather than just the mean.

In this paper and the companion paper of Scholtz et al. (2018), we build on the sample of Mullaney et al. (2015) with the observation of a larger sample of X-ray AGN covering higher X-ray hardband (HB; 2–8 keV) luminosities ($L_{2-8\,\mathrm{keV}} > 10^{44}\,\mathrm{erg\,s^{-1}}$). Here, we present a sample of 109 X-ray AGN observed with ALMA in Band-7 (i.e. 870 µm), covering the redshifts of $1 < z < 4.7$ and X-ray HB luminosities of $10^{42} < L_{2-8\,\mathrm{keV}} \leq 10^{45}\,\mathrm{erg\,s^{-1}}$. An important factor that needs to be taken into account in such studies is the possible contribution of the AGN to the FIR/sub-mm emission observed, as argued by a number of AGN studies (e.g. Mullaney et al. 2011; Del Moro et al. 2013; Leipski et al. 2013; Delvecchio et al. 2014; Netzer et al. 2016; Symeonidis et al. 2016; Stanley et al. 2017). Especially when looking at FIR faint galaxies with deep ALMA observations, where AGN contamination could have a significant effect on the measured SFR values. For this reason, we use available photometry covering 3.6–870 µm, in order to perform individual spectral energy distribution (SED) fitting and decompo-sition of the star formation and AGN contributions to the IR SED, providing SFR constraints where the AGN contamination has been removed as best as possible. The improved SFR measurements presented here are used in the companion paper of Scholtz et al. (2018) in order to define the SFR and SFR/M_* (sSFR) distributions of the AGN sample.

In Section 2, we present the sample used for this study, and give information on the ALMA observations. In Section 3, we present the IR SED-fitting method. In Section 4, we demonstrate the improvements on constraining the SFRs and identifying the AGN component of the IR SEDs that ALMA provides. In Section 5, we demonstrate the use of the $F_{870\,\mu m}/F_{24\,\mu m}$–redshift plane as a selection tool for AGN. Finally, in Section 6, we give a summary of our results. Throughout this paper, we assume $H_0 = 70\,\mathrm{km\,s^{-1}\,Mpc^{-1}}$, $\Omega_M = 0.3$, $\Omega_\Lambda = 0.7$, and a Chabrier (2003) initial mass function (IMF).

2 SAMPLE AND OBSERVATIONS

We present a sample of X-ray selected AGN that have been observed in two ALMA Band-7 programs during Cycle 1 and Cycle 2. Our ALMA Band-7 programs were designed with a key aim of constraining the SFR and sSFR distributions of a sample of X-ray AGN covering moderate to high X-ray luminosities, in the redshift range where we observe the peak of star formation and AGN activities. The details of the sample selection for the two programs are given in Scholtz et al. (2018), we give a brief overview in Section 2.1. Information on the ALMA observations and data reduction are given in Section 2.2. The complementary mid-IR (MIR) and FIR photometries for our sample are described in Section 2.3. In Section 2.4, we provide details on two comparison samples that are later used in Section 5.

2.1 Sample selection

The Cycle 1 sample was selected from the 4Ms *Chandra* Deep Field South (CDF-S) catalogue of Xue et al. (2011) to have $L_{2-8\,\mathrm{keV}} > 10^{42}\,\mathrm{erg\,s^{-1}}$ at redshifts of $1.5 < z < 3.2$ (see Mullaney et al. 2015; Harrison et al. 2016). The sample was selected to be complete for host galaxy stellar masses of $>10^{10}\,\mathrm{M_\odot}$. The Cycle 2 sample was selected from the 1.8Ms *Chandra*-COSMOS (C-COSMOS) catalogues of Elvis, Civano & Vignali et al. (2009) and Civano et al. (2012) covering the redshifts of $1.5 < z < 3.2$ and X-ray HB luminosities of $10^{43} < L_{2-8\,\mathrm{keV}} \lesssim 10^{45}\,\mathrm{erg\,s^{-1}}$, with a uniform sampling of the $L_{2-8\,\mathrm{keV}}$-redshift plane in the above ranges. The luminosity range for this selection was chosen in order to cover the knee of the X-ray luminosity function at the redshifts of interest, i.e. $L* \sim 10^{44}\,\mathrm{erg\,s^{-1}}$ at $z \sim 2$ (e.g. Aird et al. 2015), and complement the Cycle 1 sample that covered lower X-ray luminosities. The typical space densities of X-ray AGN at these luminosities and redshifts are $\sim 10^{-4}\,\mathrm{Mpc^{-3}}$ (see fig. 18 of Aird et al. 2015).

Both selections have been restricted to within the areas covered by the *Herschel* observational programs PEP/GOODS-H (Lutz et al. 2011; Elbaz et al. 2011) and HerMES (Oliver et al. 2012) in the fields of GOODS-S, and COSMOS, which are our main sources of the FIR photometry covering the observed wavelengths of 70–500 µm (described in Stanley et al. 2015). In both ALMA programs, the targeted sources were primarily chosen to have insufficient *Herschel* photometry (i.e. detected in too few *Herschel* bands) to successfully constrain the IR SED and decompose it to the star-forming and AGN components. Consequently, our sample consists of mostly *Herschel*, and sometimes *Spitzer*, undetected sources with poor SFR
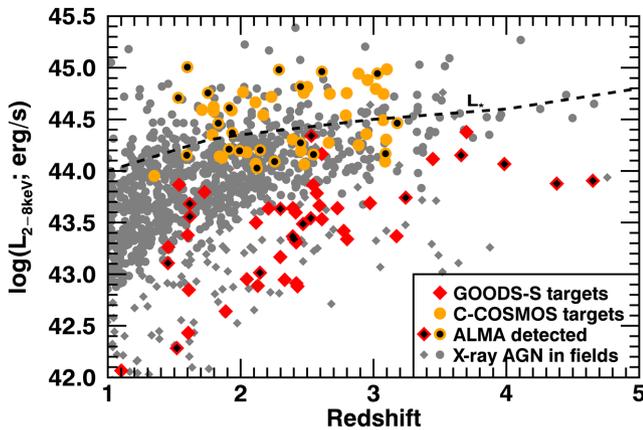
Figure 1. X-ray HB (2–8 keV) luminosity ($L_{2-8\,keV}$) as a function of redshift. In grey, we show all X-ray AGN catalogued in the GOODS-S (diamonds) and C-COSMOS (circles) fields. In colour, we show the 109 $z > 1$ X-ray AGN observed with ALMA, including 101 originally targeted and eight serendipitous detections. Detected sources are highlighted with black centres. With the dashed curve, we plot the knee of the X-ray luminosity function (L_*) from Aird et al. (2015).

constraints. We make use of the *Spitzer* and *Herschel* photometries assigned to the X-ray AGN in Stanley et al. (2015) for our analysis (see Section 2.3), in combination with ALMA observations at 870 μm. However, since the original selection of targets for our ALMA observed programs, new redshift catalogues of the CDF-S and C-COSMOS have been published by Hsu et al. (2014) and Marchesi et al. (2016), respectively. In our analysis, we make use of the updated redshifts from these catalogues.

In this paper, we analyse the X-ray AGN that were observed by ALMA, including serendipitous detections within the ALMA primary beam, with $z > 1$. This results in 109 X-ray AGN with ALMA-870 μm observations, 101 originally targeted, and eight serendipitous X-ray AGN. There are an additional five sources with $z < 1$ covered by the ALMA program, all in the field of GOODS-S, that are not included in the analysis of this paper, but their ALMA photometry and source properties are given in Scholtz et al. (2018). Our sample covers an X-ray luminosity range of $10^{42} < L_{2-8\,keV} \lesssim 10^{45}$ erg s^{-1} and a redshift range of $1 < z < 4.7$. In Fig. 1, we plot the $L_{2-8\,keV}$ as a function of redshift for the sample studied here, and highlight the ALMA-870 μm detected sources. In Fig. 1, we also plot all X-ray AGN from the catalogues used in our selection in grey, as well as the L_* track from Aird et al. (2015). It is easy to see that our sample covers almost the full luminosity range of the catalogued X-ray AGN at redshifts of $1.5 < z < 3.2$, and covers at least an order of magnitude on either side of the L_*, making it a representative sample of X-ray AGN at these redshifts. The luminosity range of our sample also covers the full range of X-ray luminosities typically included in studies of the SFR trends as a function of X-ray luminosity, and overlaps with the lower luminosities of the more luminous quasars.

2.2 ALMA-870 μm observations

The samples of 109 X-ray AGN were observed during Cycle 1 (2012.1.00869.S; PI: J. R. Mullaney) and Cycle 2 (2013.1.00884.S; PI: D. M. Alexander) with a bandwidth of 7.5 GHz centred at 351 GHz, with 55 sources in CDF-S and 54 sources in C-COSMOS. Cycle 1 observations were carried out using 32 antennas in the 12-m array and nine antennas in the 7-m array, with integration times

ranging between 2.5 and 13 min. Cycle 2 observations were carried out using 34 antennas in the 12-m array and nine antennas in the 7-m array, with integration times ranging between 1 and 6 min.

The data were processed and imaged following the methods of Hodge et al. (2013) and Simpson et al. (2015); see full details in Scholtz et al. (2018). We used the common astronomy software application (CASA; version 4.4.0; McMullin et al. 2007), and the CLEAN routine in CASA. The raw data were calibrated using the ALMA data reduction pipeline. The results were visually inspected, and when deemed necessary, the pipeline calibration process was repeated with additional data flagging. We created 'dirty' images, which were subsequently cleaned down to 3σ. We then identified the sources with S/N $\geq$ 5. To ensure the recovering of extended flux, we applied natural weighting and appropriate Gaussian tapering in the *uv*-plane to obtain a synthesized beam of $\sim$0.8 arcmin for all images. The resulting synthesized beams are of the size of (0.8–0.9 arcmin)×0.7 arcmin, with noise levels of 0.1–0.8 mJy beam^{-1} in CDF-S, and 0.08–0.23 mJy beam^{-1} in C-COSMOS. The large noise levels of 0.8 mJy beam^{-1} correspond to a subsample of 14 targets in the CDF-S field that were observed at higher resolution than that requested (i.e, 0.3 arcmin instead of 1 arcmin resolution). Therefore, for these observations, the images had to be heavily tapered to a resolution of 0.8 arcmin, resulting in increased noise levels (see Scholtz et al. 2018). This is taken into account in Section 4, when assessing the improvements in SED fitting due to ALMA photometry.

In Scholtz et al. (2018), we present the ALMA-870 μm photometric catalogues for the full sample of targeted and serendipitous X-ray AGN, along with a detailed description of the catalogue production. The catalogue includes all targeted sources and serendipitous detections. If a source remains undetected, we take 3×rms as the flux density upper limit. In total, we find that 40/109 (36.7 per cent) of our sources are detected by ALMA.

2.3 MIR and FIR photometries

For our SED-fitting analysis, we exploit available photometry in the observed frame wavelength range of 3.6–500 μm, provided by observations carried out by: *Spitzer*–IRAC at 3.6–8 μm; *Spitzer*–IRS at 16 μm; *Spitzer*–MIPS at 24 μm; *Herschel*–PACS at 70, 100, and 160 μm; and *Herschel*–SPIRE at 250, 350, and 500 μm, in addition to the ALMA photometry outlined above.

The MIR and FIR counterparts of the X-ray AGN in our sample have already been defined in Stanley et al. (2015) using the optical positions of the X-ray AGN to match to the following catalogues: *Spitzer*–IRAC sources as described in Damen et al. (2011), and Sanders et al. (2007), for GOODS-S and COSMOS, respectively; *Spitzer*–IRS 16 μm photometry from Teplitz et al. (2011) for GOODS-S; deblended catalogues of MIPS 24 μm, PACS 70, 100, and 160 μm from Magnelli et al. (2013);[1] deblended catalogues of SPIRE 250, 350, and 500 μm from Swinbank et al. (2014).

All the IRAC catalogues have their detections determined by the 3.6 μm maps, the 16 μm catalogues, and the 24 μm deblended catalogues have been produced with the use of 3.6 μm priors. The PACS and SPIRE deblended catalogues have been produced using the deblended 24 μm catalogues as priors. Although in principle

---

[1]The PACS catalogues for and GOODS-S are published in Magnelli et al. (2013). The catalogue for COSMOS was created in the same way and is available online (http://www.mpe.mpg.de/ir/Research/PEP/DR1).

we have defined photometry for the full range of 3.6–870 µm, due to the redshifts covered by our sample the SED-fitting analysis used in our work only makes use of photometry for 24–870 µm, for the majority of the sources.

2.4 Comparison samples of AGN-dominated and star-forming galaxies

In Section 5, we make use of three $z > 1$ galaxy samples with published 870 µm ALMA photometry, in order to explore the $F_{870\,\mu m}/F_{24\,\mu m}$-redshift plane. In addition to the X-ray AGN sample of this paper, we use two extreme samples representative of AGN-dominated sources (radio powerful MIR AGN), and star-forming galaxies (sub-mm galaxies; SMGs). Here we provide some more information on these two samples.

The first comparison sample is that of AGN-dominated sources. The sample consists of AGN-dominated galaxies taken from Lonsdale et al. (2015), covering the redshifts $0.47 < z < 2.85$, and selected to have ultrared *WISE* colours and to be radio loud. These are sources lying significantly redward to the main *WISE* population in the (W1–W2) versus (W2–W3) colour space, where W1 corresponds to 3.4 µm, W2 to 4.6 µm, W3 to 12 µm, and W4 to 22 µm. Samples of sources selected to be the reddest sources in the *WISE* colour plane have been revealed to be an IR-luminous population of high-redshift galaxies with strong AGN (e.g. Eisenhardt et al. 2012; Bridge et al. 2013; Jones et al. 2014; Tsai et al. 2015), and IR luminosities likely dominated by the AGN emission (e.g. Jones et al. 2015). Lonsdale et al. (2015) present ALMA observations and measurements of 870 µm of 49 such sources, with a resolution of 0.5–1.2 arcmin, and noise levels of 0.3–0.6 mJy beam^{-1}, comparable to the ALMA photometry of our sample. Based on Lonsdale et al. (2015), this sample has AGN bolometric luminosities of the order of 10^{46} erg s^{-1}, covering the high end of AGN luminosities, and has been selected to be radio loud. Furthermore, Lonsdale et al. (2015) estimate the possible contribution from optically thin synchrotron emission to the ALMA flux density using multifrequency Very Large Array data, and argue that none of the sources have strong contamination in their ALMA flux densities. We use 41 (out of the 49 sources) constrained to redshifts of $z > 1$, with complementary *WISE* photometry. The redshifts of the sample are primarily spectroscopic, except for four sources with no redshift for which the authors assume that $z = 2$.

The second comparison sample is that of star-forming galaxies, and consists of SMGs. SMGs represent the highly star-forming population at high redshifts, $z \sim 2$–3 (e.g. Blain et al. 2002; Wardlow et al. 2011; Casey et al. 2013), with typical IR luminosities of $L_{IR} \sim 10^{46}$ erg s^{-1} (e.g. Swinbank et al. 2014) dominated by emission due to star formation. The chosen sample of SMGs is taken from the ALMA–LESS survey (A-LESS; Hodge et al. 2013; Karim et al. 2013), including 122 sources over the redshift range of $0.4 < z < 7$ observed with ALMA-870 µm during Cycle 0. Spectroscopic redshifts where taken from Danielson et al. (2017), photometric redshifts and NIR photometry from Simpson et al. (2014), and MIR and FIR photometries from *Spitzer*–MIPS and *Herschel* from Swinbank et al. (2014). In total, we use 113 sources of the sample constrained to redshifts of $1 < z < 5$ (covering a similar redshift range as our sample of X-ray AGN), with spectroscopic redshifts for 51 of the sources, the rest being photometric. For the ALMA observations of this sample, the median resolution was ∼1.4 arcmin, and reach typical noise levels of 0.4–0.5 mJy beam^{-1}, comparable to the ALMA photometry of our sample. Although the majority of SMGs is known to be dominated by emission due to star formation, they can still be

hosts to AGN. Wang et al. (2013) presented the X-ray counterparts for part of the A-LESS sample, finding that 8 out of the 91 SMGs included, are hosts to X-ray AGN. There have been a number of previous studies identifying AGN in SMG samples in both the MIR (e.g. Valiante et al. 2007; Pope et al. 2008; Coppin et al. 2010) and X-ray (e.g. Alexander et al. 2005; Laird et al. 2010). The X-ray AGN identified in the A-LESS sample have X-ray Full Band, 0.5–8 keV, luminosities of 10^{42}–$10^{44.5}$ erg s^{-1} (Wang et al. 2013). We discuss the AGN in this sample further in Section 5.2.

3 IR SED FITTING AND DECOMPOSITION

We performed fitting and decomposition of the IR SED by following and extending the methods of Stanley et al. (2015). The SED-fitting procedure makes use of a set of empirical templates describing the IR star formation and AGN emission, in order to decompose the SED into the star formation and AGN components. The set of templates consists of six star-forming galaxy templates and an AGN template (we explore other AGN templates below). This includes the five star-forming galaxy templates originally defined in Mullaney et al. (2011, later extended in wavelength by Del Moro et al. 2013), with the addition of Arp220 from Silva et al. (1998), and the mean AGN template defined in Mullaney et al. (2011) from a sample of X-ray AGN. We asses the impact of our AGN template choice on the SED fitting later in this section, and how it compares to other templates in colour–redshift space in Section 5.

Following Stanley et al. (2015), we performed two sets of SED fitting to photometry at 8–870 µm. The first set includes only the star-forming galaxy templates in the fit, while the second set includes both the AGN and star-forming components. We fit to the photometric flux density detections, but also force the fits to not exceed any of the photometric flux density upper limits. This procedure results in 12 fitted SEDs to chose from, six with and six without the AGN components. We calculate the integrated 8–1000 µm IR luminosity due to star formation from the host galaxy ($L_{IR,SF}$) and due to the AGN ($L_{IR,AGN}$), for each of the 12 fitted SEDs. To determine the best-fitting solution of the 12 fitted SEDs, we use the Bayesian Information Criteria (BIC; Schwarz 1978) which allows the objective comparison of different non-nested models with a fixed data set. The SED fit with the minimum BIC value is defined as the best fit. However, to establish if the SED of the source requires an AGN component, the SED with the AGN component has to have a smaller BIC than that of the SED with no AGN component with a difference of ΔBIC >2. This difference establishes a significant improvement on the fit by the inclusion of the AGN component. The uncertainties on the chosen $L_{IR,SF}$, and $L_{IR,AGN}$ values are the combination of the formal error on the fit and the range of $L_{IR,SF}$ and $L_{IR,AGN}$ values covered by all template combination fits with ΔBIC <2 to the best fit (see Stanley et al. 2015).

Our fitting results in one of five different situations depending on the number of photometric bands a source is detected in. We detail how we chose the best fit for each below:

(i) If we have more than two photometric detections and at least one is within the FIR range of the rest-frame SED (i.e. at rest-wavelength greater than ∼80 µm where the peak of star formation emission starts), we are able to decompose the AGN and star formation emission effectively. Therefore, we chose the fit with the minimum BIC value as our best fit. If multiple fits have the same value as the minimum BIC, then we take the mean $L_{IR,SF}$, and $L_{IR,AGN}$ of those fits (e.g. Fig. 2a).
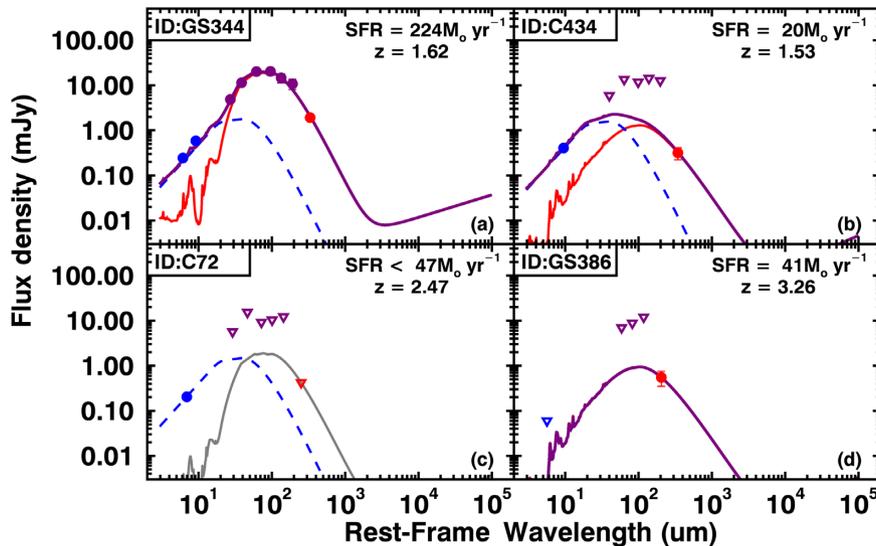
Figure 2. Examples of four different cases of SED-fitting results. In all cases, the blue dashed curve is the AGN component, while the red solid curve is the star-forming component. The total combined SED is shown as a purple solid curve. The grey curves correspond to an upper limit constraint on the SF component. The photometry is colour-coded, with blue corresponding to *Spitzer* bands, purple to *Herschel* bands, and red to the ALMA-870 μm photometry. The inverse triangles are upper limits on the flux density. (a) An example where we have full photometric coverage of the SED [see case (i) in Section 3]. In this case, the ALMA photometry on the SED provides confidence in the SED templates used for our analysis. (b) An example where the source is only detected in MIPS-24 μm and ALMA-870 μm [see case (ii) in Section 3], and (c) an example of an ALMA undetected source that is only detected in the MIR [see case (v) in Section 3]. In both cases of (b) and (c), the deep ALMA photometry, allow us to constrain the star-forming component to a level that reveals the presence of an AGN component in the MIR. (d) An example were the source is undetected in all bands except for ALMA-870 μm [see case (iii) in Section 3]. In the last case, we are confident that the emission is dominated by star formation, as a significant contribution from the AGN the source would result in an MIR detection, which is not the case.

(ii) If a source is only detected in the MIPS-24 μm and ALMA-870 μm band, we use the comparative BIC values to decide if the IR SED requires the AGN component or not. However, we are unable to discriminate between the different star formation templates. Therefore, we take the mean $L_{IR,SF}$, and $L_{IR,AGN}$ for the set of fits that best describe the SED (e.g. Fig. 2b).

(iii) If a source is only detected in the ALMA-870 μm band, we are unable to discriminate between the star formation templates. Therefore, we normalize the star-forming galaxy templates to the ALMA photometry and take the mean of the resulting $L_{IR,SF}$ for the full template range. We are confident that if the AGN was significantly contributing to the ALMA photometry, it would have been detected in the MIR at the depth of the MIPS-24 μm photometry. Based on the shape of the AGN IR SED, if the AGN was detected at the detection limit of the 24 μm flux density (0.06 mJy), it would emit $\sim 6 \times 10^{-4}$–0.1 mJy at 870 μm from redshift 1 to 4.7, respectively. The highest contribution possible by the AGN to the 870 μm flux density, for the sources in our sample, would be at a redshift 4.7, and would only account for ~ 6 % of the measured flux density of the source at that redshift. An example of this is given in Fig. 2(d), where we show the case of a $z = 3.26$ galaxy detected only at 870 μm. If the AGN was to emit the observed 870 μm flux density of 0.4 mJy, then the 24 μm flux density should be ~ 4 mJy, a value significantly larger to that of the flux density limit.

(iv) If a source has only MIR detections, or no detections at all, then we cannot confidently decompose the SED and so we constrain an upper limit on the star-forming component using the limits and/or the 3σ error on the detections. We normalize all star-forming templates to the lowest value of the upper limits, including as a limit the 3σ above the photometry if the source is detected in a given MIR band. We then take the maximum $L_{IR,SF}$ value of the

range of normalized templates, as the upper limit. The same is done for the estimation of the $L_{IR,AGN}$ upper limit.

(v) If a source is detected in the MIR and the limit on the star-forming component (constrained by the limits at > 80 μm) is $>5\sigma$ below the observed frame 8–24 μm photometry, then we can identify the presence of an AGN component. We find that in these cases, we can measure the $L_{IR,AGN}$, even if we can only constrain an upper limit on the $L_{IR,SF}$ (e.g. Fig. 2c).

Following this method, we have performed individual SED fitting for the whole sample of X-ray AGN studied here. The results from the SED-fitting procedure are given in Tables A1 and A2 along with the X-ray HB luminosity ($L_{2-8\,keV}$) and redshift (z) of the sources. The best-fitting SEDs for all sources are given in Fig. A1. Interestingly, where we could only identify a MIR AGN component in one of our sources prior to ALMA observations, we can now confidently identify a MIR AGN component in 54/109 (~ 50 %) of the ALMA observed sample, with AGN fractions down to 20 % of the total IR (8–1000 μm) luminosity. Throughout this paper, we only consider that a source has a MIR AGN component in their SED when the fit requires an AGN component with a significant contribution (at least 20%), while SED fits that require an AGN component with a very weak contribution (less than 20 %) are considered uncertain. These sources are flagged in Tables A1 and A2, with a flag of 1 for weak/uncertain AGN components in the fit, and a flag of 2 for fits with a significant AGN component.

We note that a comparison between the observed $L_{2-8\,keV}$ values and the measured 6 μm luminosities from the AGN component of our SED fits (when present), shows a good agreement between the two. Specifically, the majority of the sources with an AGN component in their SED fits lie within the scatter of the local AGN relation (e.g. Lutz et al. 2004). There is one source lying sig-

nificantly offset from the local relation. This source has an observed $L_{2-8\,keV}$ value lower than the 6 µm luminosity by 1.6 dex(factor of ∼40), which is consistent with the measured column density of $N_H = 9 \times 10^{23} cm^{-2}$ (from Luo et al. 2017).

We have followed the same SED-fitting method for the two comparison samples described in Section 2.3, using the available published photometry. Overall, with our SED-fitting procedure, we have an $L_{IR,SF}$ measurement for 21/41 (51 %) of the AGN-dominated sources with the rest having a well-constrained upper limit. As expected, we identify an AGN component in all 41 of the AGN-dominated sources with a minimum AGN contribution to the total IR luminosity of 50 %, and with 22/41 (54 %) of the sample having an AGN component that contributes $\gtrsim$90 % of the IR luminosity. When looking at the star-forming galaxy sample, our SED-fitting process can constrain an $L_{IR,SF}$ measurement for the whole sample, and finds that all of the sources have IR emission dominated by star formation, with only 12/113 (11 %) of the sources having an identified IR AGN component. The $L_{IR,SF}$ values of these comparison samples cover the range of ∼0.2–3×10^{47} erg s^{-1} and ∼0.2–4×10^{46} erg s^{-1} for the AGN-dominated and star-forming galaxies, respectively (see also Tables A3 and A4).

In our analysis, we have only used one AGN template, that of Mullaney et al. (2011) defined for a sample of nearby X-ray AGN. However, there is a number of other AGN templates defined for different samples (e.g. Mor & Netzer 2012; Symeonidis et al. 2016; Lani, Netzer & Lutz 2017; Lyu & Rieke 2017). Since many of our sources are found to have a strong AGN component in their IR SED, we need to test if the results are affected by the choice of AGN template. The most deviant AGN template from our primary choice is that of Symeonidis et al. (2016), defined for a sample of optical Palomar Green (PG) quasars. This template can have a stronger IR contribution than that of Mullaney et al. (2011), due to the fact that it is characterized by a more gradual drop-off at long wavelengths. However, recent work by Lani et al. (2017) and Lyu & Rieke (2017) have demonstrated that for the same or similar samples of PG quasars the AGN template derived is actually much more similar to that of Mullaney et al. (2011), than Symeonidis et al. (2016), shedding some uncertainty on the later template. Furthermore, when we examine the $F_{870\,µm}/F_{24\,µm}$–redshift plane in Section 5, we demonstrate that the Symeonidis et al. (2016) template is inconsistent with the colours of most AGN dominated sources. Finally, using the AGN templates with a steeper drop-off at the longer wavelengths, has a minimal effect on our derived SFRs, typically at only a few per cent level (see Stanley et al. 2015, 2017).

4 IMPROVEMENTS ON $L_{IR,SF}$ CONSTRAINTS

To demonstrate how much better we can constrain $L_{IR,SF}$ for our sample once we have ALMA photometry in addition to *Spitzer* and *Herschel*, we have performed the same SED-fitting analysis on the sample with and without the ALMA photometry. Here, we quantify the improvements achieved on the $L_{IR,SF}$ values.

In Fig. 3 (left), we show $L_{IR,SF}$ when constrained using 8–500 µm photometry (purple) and 8–870 µm (red) photometry (i.e. without and with the ALMA photometry), as a function of redshift. For comparison, we also plot the track for the mean $L_{IR,SF}$ of star-forming main-sequence galaxies (e.g. Schreiber et al. 2015) with stellar masses of $M_* = 10^{11}$ $M_\odot$ (the rounded median stellar mass for our sample; Scholtz et al. 2018). In Fig. 3 (right), we show a different representation of the comparison, by plotting the new $L_{IR,SF}$ values constrained with the additional ALMA photometry ($L_{IR,SF}^{alma}$) against original $L_{IR,SF}$ values constrained without the ALMA pho-

tometry ($L_{IR,SF}^{orig}$). With a dashed line, we give the 1-to-1 ratio. As the sample was selected to be *Herschel* undetected/FIR faint, the majority of the sources (107/109; 98 %) only had upper limit constraints on their $L_{IR,SF}$ values in the absence of the ALMA 870 µm photometry. The ALMA photometry allows us to both measure the $L_{IR,SF}$ of sources not possible previously (from 2 to 37 % of the sample), and to also push the limits on $L_{IR,SF}$ values to significantly lower levels, up to a factor of 10 (see Figs 3 and 4). For sources with sufficient *Herschel* constraints to measure $L_{IR,SF}$ (2/109), we find a change in $L_{IR,SF}$ when including the ALMA photometry of only a factor of 1.3 and 1.4. The agreement of the ALMA photometry to the *Herschel* constraints provides extra confidence in our SED-fitting approach and choice of templates, even in the absence of ALMA photometry.

In Fig. 4, we show a histogram of the improvement in constraining the $L_{IR,SF}$ values of the 98 % of our sample that originally only had upper limit constraints based on *Herschel* photometry. The value plotted is given by the equation: $\frac{L_{IR,SF}^{orig} - L_{IR,SF}^{alma}}{L_{IR,SF}^{orig}}$. With the filled regions of the histogram, we highlight the sources that turned from upper limits to measurements. It is immediately clear that more than half of our sample (67%) have $L_{IR,SF}$ constraints that have changed by more than a factor of 2. The apparent bimodality in the improvements of the upper limit constraints is driven by the range of rms values for our observations. For the subsample of 14 sources incorrectly observed with high resolution, the resulting rms of the heavily tapered ALMA maps is as high as 0.8 mJy beam^{-1}, which results in only a small improvement on the constraints of the $L_{IR,SF}$ upper limits (see Section 2.1; Scholtz et al. 2018).

Overall, we now have $L_{IR,SF}$ measurements for 40/109 (≃37%) of the sources, that is 20 times more sources than what was possible without the ALMA photometry. For the sources that still have an upper limit constraint (69/109; ≃63 %), the values have lowered by up to a factor of 10 with the addition of ALMA data. Furthermore, the majority of our sample (67 %) have improved by more than a factor of 2, and we can now identify an AGN component in the IR SEDs of 50 % of our sample compared to the original 0.9 %. In summary, we have demonstrated that deep (∼0.1–0.3 mJy) 870 ALMA observations, in combination with *Spitzer* and *Herschel* data, significantly improve the AGN–star formation SED decomposition and SFR measurements for distant X-ray AGN. Such improvements make it possible to constrain SFR distributions of this population rather than just investigate mean properties (Mullaney et al. 2015; Scholtz et al. 2018).

5 THE AGN IR EMISSION: IDENTIFYING AGN THROUGH THEIR $F_{870\,µm}/F_{24\,µm}$ RATIO

With the excellent constraints on the star formation component of the IR SED that the ALMA observations can provide, we are now able to better constrain the MIR emission of the AGN itself. The shape of the star-forming IR SED, in combination with the constraints placed on it by the ALMA 870 µm photometry, allows for the detection of a MIR excess, even when a source is undetected at 870 µm. Indeed, as mentioned in Section 3, we can now confidently identify a MIR AGN component in ∼50 % of the ALMA observed sample, with AGN fractions down to 20 % of the total IR luminosity.

The deepest data in the extragalactic deep fields, such as CDF-S and COSMOS, within the wavelength range of the IR SED are from 24 µm (*Spitzer*–MIPS) and 870 µm (ALMA Band-7) observations. For a composite source, that has both AGN and star formation
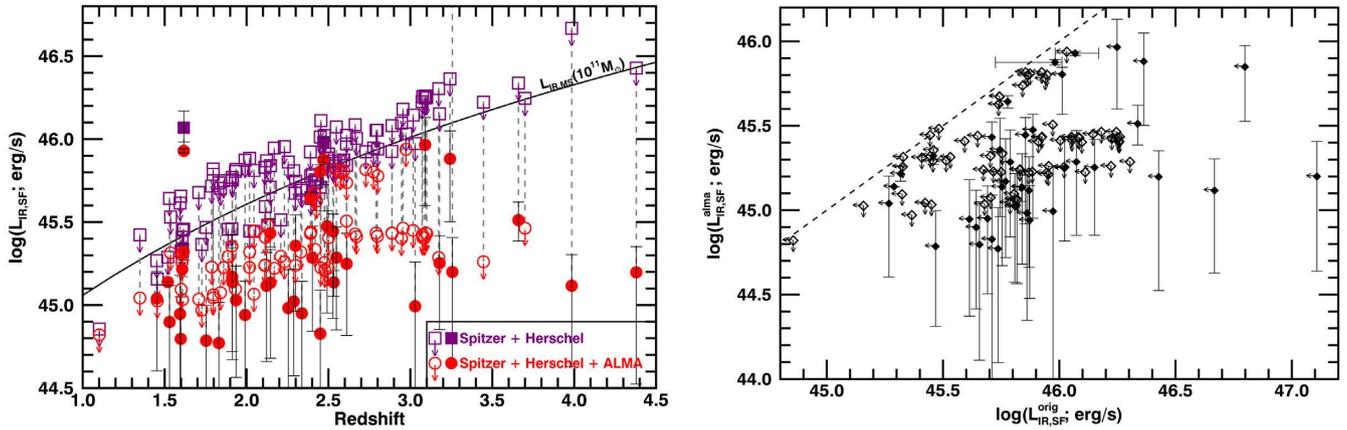
Figure 3. *(Left)*: IR luminosity due to star formation ($L_{IR,SF}$) as a function of redshift for our sample before (purple) and after (red) the inclusion of deep ALMA photometry in our SED fitting. *(Right)*: IR luminosity due to star formation after the inclusion of the ALMA photometry ($L_{IR,SF}^{alma}$) as a function of the IR luminosity due to star formation before the inclusion of the ALMA photometry ($L_{IR,SF}^{orig}$), with the dashed line corresponding to the 1-to-1 ratio. We now have 20 times more measurements than previously possible, with 40/109 sources having an $L_{IR,SF}$ measurement. For 73/109 (67 %) of the sources, the measurements and upper limit constraints on $L_{IR,SF}$ have typically decreased by factors of 2–10 compared to the original upper limit constraints (see Fig. 4).
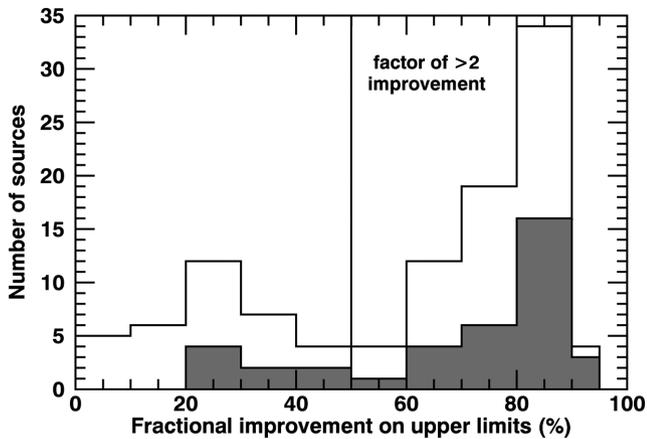
Figure 4. Histogram of the improvement in the $L_{IR,SF}$ values and upper limits when ALMA photometry was included (*alma*), compared to the original upper limit constraints (*orig*), i.e. ($L_{IR,SF}^{orig} - L_{IR,SF}^{alma}$)/ $L_{IR,SF}^{orig}$. Filled in black are the values corresponding to sources that turned from upper limits in the original fit, to measurements when including the ALMA photometry. The majority of the upper limits in our sample (73/109) have new $L_{IR,SF}$ measurements or upper limits that have decreased by more than a factor of 2. We note that from the remaining 36/109 sources that have less than a factor of 2 improvements, 14 where observed in the wrong configuration. As a consequence, these 14 sources have larger rms values than the rest of the sample (see Section 2.1; Scholtz et al. 2018).

emissions in the IR, having detections and/or deep upper limits of the flux density at those wavelengths may allow for a successful decomposition of the AGN and SF components. For this reason, we explore the parameter space of the ratio of the flux densities at 870 μm over 24 μm as a function of redshift, for the potential of identifying AGN-dominated and composite sources. Throughout the rest of this paper, we call this the $F_{870\,\mu m}/F_{24\,\mu m}$-redshift plane, where $F_{870\,\mu m}$ is the flux density of the ALMA Band-7 at 870 μm and $F_{24\,\mu m}$ is the flux density of the *Spitzer*–MIPS 24 μm band. In order to do this, we use three different samples: (1) the X-ray AGN sample of this study that mostly contains composite sources; (2) an AGN-dominated galaxy sample; and (3) a star-forming galaxy

sample (see Section 2.4). We have chosen the two additional samples in order to cover the two extremes of AGN-dominated IR SEDs, and star formation-dominated IR SEDs, as well as the range of composites between them. Samples (2) and (3) are described in Section 2.4.

In Section 5.1, we use the SED templates for the AGN and SF components in order to define the $F_{870\,\mu m}/F_{24\,\mu m}$-redshift plane, and use the three galaxy samples to verify the AGN, star formation, and composite regions. In Section 5.2, we compare the selection of AGN candidates based on the $F_{870\,\mu m}/F_{24\,\mu m}$ ratio, to the findings from our SED-fitting analysis, and to existing IRAC colour selection criteria.

5.1 Defining the $F_{870\,\mu m}/F_{24\,\mu m}$ -redshift plane for infrared AGN identification studies

We define the regions of the $F_{870\,\mu m}/F_{24\,\mu m}$-redshift plane dominated by purely AGN emission and by purely star-forming emission using the star-forming templates of our SED-fitting procedure, and the AGN templates of Mullaney et al. (2011), the mean of which is used in our SED-fitting procedure (see Section 3). For comparison and to explore the $F_{870\,\mu m}/F_{24\,\mu m}$-redshift plane, we also include an additional two AGN templates, and an additional set of SF templates. We use the set of star-forming templates from Dale & Helou (2002) produced by a phenomenological model of star-forming galaxies, and the AGN templates of Mor & Netzer (2012) and Symeonidis et al. (2016) derived for samples of luminous quasars that cover the extremes in FIR/MIR colours for AGN templates from the literature.

We plot the $F_{870\,\mu m}/F_{24\,\mu m}$-redshift plane for the three different samples in Figs 5 and 6. With coloured regions, we show the parameter space covered by the star-forming templates (the Mullaney et al. 2011+Arp220 set of templates in pink; the set of templates from Dale & Helou 2002 in grey), and the region covered by AGN templates (from Mullaney et al. 2011 in pink; Mor & Netzer 2012 in grey; and Symeonidis et al. 2016 in blue). We note that the template of Mor & Netzer (2012) is limited to redshifts of $z \geq 2.7$ in our plots, due to the restricted wavelength region (0.5–250 μm) it has been defined for. There is a clear divide between the regions covered by the star formation and AGN templates. This is due to the relative
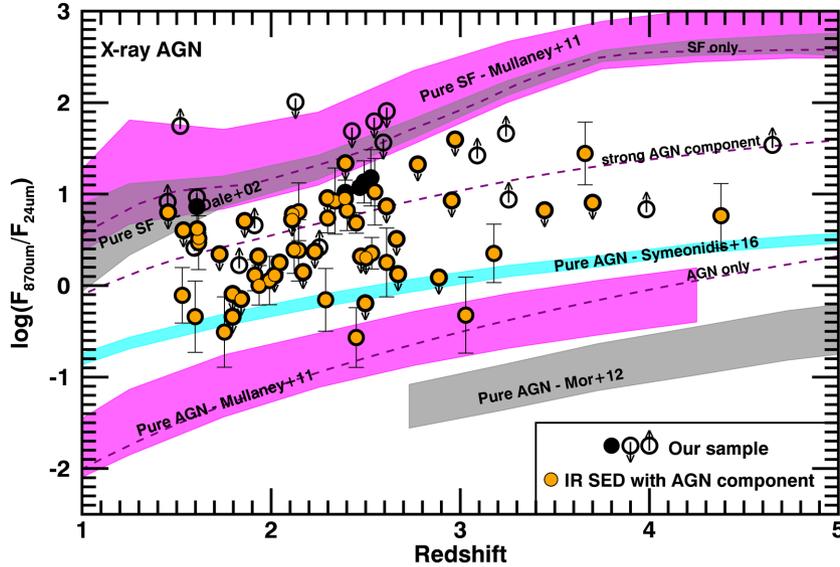
Figure 5. The $F_{870\,\mu m}/F_{24\,\mu m}$ ratio as a function of redshift for the ALMA observed sample of X-ray AGN. Sources for which our SED fitting finds an AGN component with more than 20 % contribution to the IR emission are highlighted with yellow centres. The purple dashed curves correspond to the median $F_{870\,\mu m}/F_{24\,\mu m}$ ratio as a function of redshift for SEDs with 0 % AGN contribution (SF only), 50 % AGN contribution (strong AGN component), and 100 % AGN contribution (AGN only) to the IR luminosity.

shapes of the AGN and star formation IR SEDs (see blue dashed and red solid curves in Fig. 2), which results in sources with a significant contribution from the AGN component having a 24 μm flux density dominated by the AGN emission, while the 870 μm flux density will be dominated by the star formation (except for cases of pure AGN emission).

When plotting the X-ray AGN sample that consists of a wide range of AGN – SF composite sources, it covers the full range between the star formation and AGN region of the plane (see Fig. 5). This is not surprising as the X-ray sample covers a broad range of X-ray luminosities, and there can be a wide range of SFR values for a fixed AGN luminosity in samples of X-ray AGN (e.g, Mullaney et al. 2015; see section 4.3 of Stanley et al. 2015). To test if the star formation and AGN regions of the plane are indeed representative of star-forming galaxies and AGN-dominated sources, we use the two samples described in Section 2.4, one representative of AGN dominated sources, and one representative of star-forming galaxies. In Fig. 6, we plot the $F_{870\,\mu m}/F_{24\,\mu m}$-redshift plane for these two samples. The AGN-dominated sample lies at $F_{870\,\mu m}/F_{24\,\mu m} < 1.6$ and towards the AGN region of the plane. The star-forming galaxy sample lies at $F_{870\,\mu m}/F_{24\,\mu m} > 1.6$ and towards the star formation region of the plane. The agreement between the colours of the AGN-dominated, and star-forming galaxies and our templates is an additional indication for their suitability for our SED-fitting analysis.

We compare the AGN-dominated sample to the regions of the plane covered by the different AGN templates, in order to asses how compatible or incompatible these AGN templates are with the observed $F_{870\,\mu m}/F_{24\,\mu m}$. Sources with $F_{870\,\mu m}/F_{24\,\mu m}$ ratios on and above those of an AGN template are considered compatible with it, while sources with $F_{870\,\mu m}/F_{24\,\mu m}$ ratios below those of the AGN template are incompatible. This is due to the fact that a $F_{870\,\mu m}/F_{24\,\mu m}$ ratio below that of a given AGN template simply cannot be described by that template, while a $F_{870\,\mu m}/F_{24\,\mu m}$ ratio above can be described as a composite of the AGN template and star formation emission. We find that the AGN template of Mullaney

et al. (2011) is compatible with 40/41 sources, the Mor & Netzer (2012) template is likely compatible with all 41.[2] In contrast, 28/41 sources lie below the $F_{870\,\mu m}/F_{24\,\mu m}$ ratios of the Symeonidis et al. (2016) AGN template, by an average factor of ∼2. Consequently, the Symeonidis et al. (2016) AGN template is the most incompatible to the $F_{870\,\mu m}/F_{24\,\mu m}$ ratios of the AGN-dominated sample.

To further quantify the location of AGN candidates in the $F_{870\,\mu m}/F_{24\,\mu m}$-redshift plane, we make use of the SED templates used in our SED-fitting analysis (see Section 3), in order to create composite SEDs with a specific AGN contribution. We use these to define the expected $F_{870\,\mu m}/F_{24\,\mu m}$ ratio as a function of redshift for composites with a strong (50%) AGN contribution to the IR luminosities, in order to distinguish different AGN contributions within the composites region of the $F_{870\,\mu m}/F_{24\,\mu m}$-redshift plane. We combine each SF template to our AGN template to create composite SEDs with a 50 per cent AGN contribution to the total IR luminosity. We then take the median composite SED. This SED is then shifted with redshift steps of 0.2 from redshifts 1 to 5, and at each step, we calculate the observed frame $F_{870\,\mu m}/F_{24\,\mu m}$ ratio. As a result, we have a measure of the median $F_{870\,\mu m}/F_{24\,\mu m}$ ratio as a function of redshift, for SEDs with a strong AGN component. We show the expected $F_{870\,\mu m}/F_{24\,\mu m}$ ratio as a function of redshift for sources with a 50 % AGN contribution to the IR luminosity in Figs 5–7, with a dashed purple track labelled 'strong AGN component', which follows the form:

$$\log_{10}\left(\frac{F_{870\,\mu m}}{F_{24\,\mu m}}\right) = -1.19 + 3.623 \times \log_{10}(1 + z) \qquad (1)$$

In Figs 5–7, we also show the median $F_{870\,\mu m}/F_{24\,\mu m}$ ratio as a function of redshift for only the star formation components, and for

---

[2]Due to the truncation of the Mor & Netzer (2012) template at 250 μm, we only calculate the $F_{870\,\mu m}/F_{24\,\mu m}$ ratio from redshifts $z > 2.7$ (plotted with a grey region in Figs 5–7). However, with simple extrapolation to lower redshifts, we can expect that all AGN-dominated sources are compatible with the template.
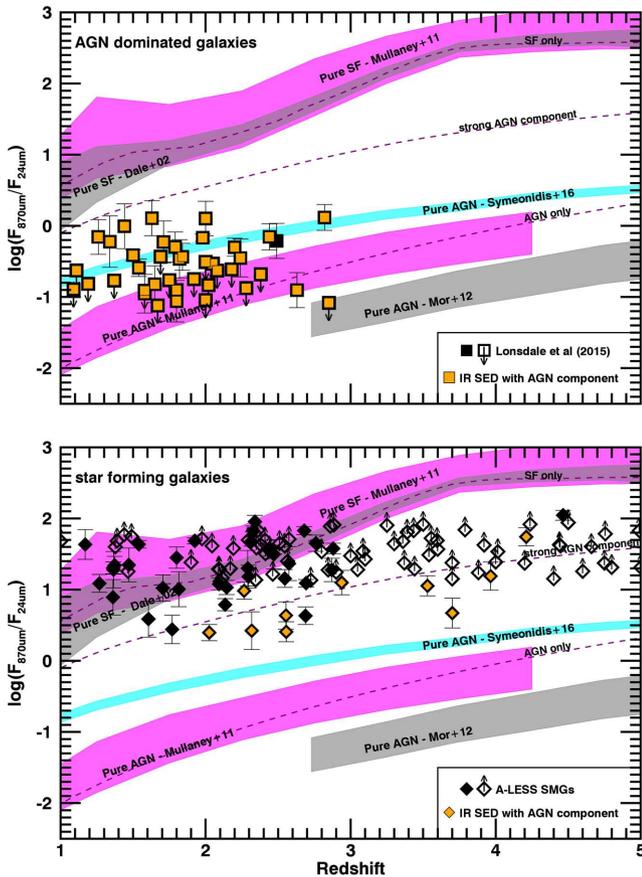
Figure 6. The $F_{870\,\mu m}/F_{24\,\mu m}$ ratio as a function of redshift, for two comparison samples also observed with ALMA. *(Top)*: the sample of AGN-dominated sources from Lonsdale et al. 2015. *(Bottom)*: a sample of SMGs from the A-LESS survey (e.g. Hodge et al. 2013). Sources for which our SED fitting finds an AGN component with at least 20 % contribution to the IR emission (flagged with 2 in Tables A3 and A4), are highlighted with yellow centres. The purple dashed curves correspond to the median $F_{870\,\mu m}/F_{24\,\mu m}$ ratio as a function of redshift for SEDs with 0 % AGN contribution (SF only), 50 % AGN contribution (strong AGN component), and 100 % AGN contribution (AGN only) to the IR luminosity. The strong AGN component curve seems to separate well the $F_{870\,\mu m}/F_{24\,\mu m}$-redshift plane in the two regions covered by star-forming galaxies and AGN-dominated sources. For this reason, we test it as an AGN candidate selection limit in Section 5.2.

only the AGN component, with dashed purple tracks labelled 'SF only' and 'AGN only' respectively.

The track defined for a strong AGN component seems to discriminate well between the two samples of AGN and star-forming galaxies, except for eight sources of the star-forming galaxy sample (see Fig. 6). These eight sources appear to have AGN signatures at various wavelengths (see Section 5.2 for further discussion). In the next subsection, we discuss the potential of using equation (1) as a method for identifying sources with strong MIR AGN emission.

5.2 AGN identification: application of a $F_{870\,\mu m}$ / $F_{24\,\mu m}$ selection and comparison to other approaches

The strong AGN component line defined in the previous section does a good job of discriminating between AGN-dominated and SF-dominated samples (see Fig. 6), and can select composite sources with a strong (>50%) AGN contribution to the IR emission. Here

we use equation (1), that describes the strong AGN component line, as the $F_{870\,\mu m}/F_{24\,\mu m}$ selection limit for AGN candidates, and compare to MIR selection methods (e.g. Stern et al. 2005; Donley et al. 2012) and the results of our SED-fitting analysis. We note that the following discussion is limited to X-ray AGN that are *Herschel* faint or non-detected based on our sample selection (Section 2.1). This sample selection may contribute to the low number of sources detected in all four IRAC bands (50/109; 46 % of the sample). In order to do the comparison to the MIR colour selection, we restrict our X-ray AGN sample to only those 50 sources. We also restrict the star-forming galaxy sample to 81/113 sources detected in all four IRAC bands.

In the case of our X-ray AGN sample, the $F_{870\,\mu m}/F_{24\,\mu m}$ limit selects 22/50 sources as AGN candidates. Of these 22 sources, all have a strong AGN component in their best-fitting SEDs. To see how many would be selected by the more commonly used MIR colour selection, we use the Donley et al. (2012) IRAC colour criteria for identifying MIR AGN, that have the lowest contamination from non-AGN sources compared to previous IRAC selection criteria (e.g. Stern et al. 2005). The IRAC colour criteria select 19 out of the 22 sources selected by the $F_{870\,\mu m}/F_{24\,\mu m}$ limit. In Fig. 7, we show the two selection methods, with the $F_{870\,\mu m}/F_{24\,\mu m}$–redshift plane shown in Fig. 7 *(left)*, and the IRAC colour–colour plane in Fig. 7 *(right)*. We note that there are five sources selected by the IRAC colour criteria that have not been selected by the $F_{870\,\mu m}/F_{24\,\mu m}$ limit. This is due to the fact that these sources have AGN components with a contribution of 0–47 % to the total IR luminosity, and by definition the $F_{870\,\mu m}/F_{24\,\mu m}$ limit discussed here will select only sources with >50 % AGN contribution. Overall, both methods are comparable in selecting sources with a strong AGN component, but both will miss the majority of sources that have AGN components contributing <50% to the total IR luminosity.

In the case of the AGN-dominated sample, the $F_{870\,\mu m}/F_{24\,\mu m}$ selection limit successfully selects the full sample of 41 sources. These sources have been selected through their *WISE* colours, and so all of them are already IR colour selected, and all 41 sources have a strong AGN component in their best-fitting SEDs.

In the case of the star-forming galaxy sample, the $F_{870\,\mu m}/F_{24\,\mu m}$ selection limit selects 8/81 sources as having a strong AGN component. Of these eight sources, seven have a confident AGN component in their best-fitting SEDs (contributing 30–83 % to the IR luminosities), and one would also be selected by their IRAC colours based on the Donley et al. (2012) criteria. Of the eight sources selected, seven have good optical spectra (Danielson et al. 2017) and/or X-ray photometry (Wang et al. 2013), and three of these show AGN signatures in the optical or X-ray. Overall, seven out of the eight sources show a significant AGN signature from additional data (including SED fitting to multiwavelength photometry). The remaining one source with none of the above-mentioned signatures has a spectroscopic redshift of tentative quality (Danielson et al. 2017), but does show a radio excess at 1.4 GHz (based on flux density measurements in Swinbank et al. 2014). It is not surprising that we find SMGs hosting AGN, as mentioned in Section 2.4, it is not uncommon for SMGs to exhibit AGN signatures. In addition to the sources discussed above, there are seven sources that have been classified as hosts of X-ray AGN (Wang et al. 2013) that are not selected by the $F_{870\,\mu m}/F_{24\,\mu m}$ selection limit, with five of them lying in the composite region of the $F_{870\,\mu m}/F_{24\,\mu m}$–redshift plane (but above the selection limit), and two lying on the star formation region. The range of $F_{870\,\mu m}/F_{24\,\mu m}$ ratios of the SMGs with identified X-ray AGN, is not surprising given the range we have already observed for the main sample of X-ray AGN in this work, and the
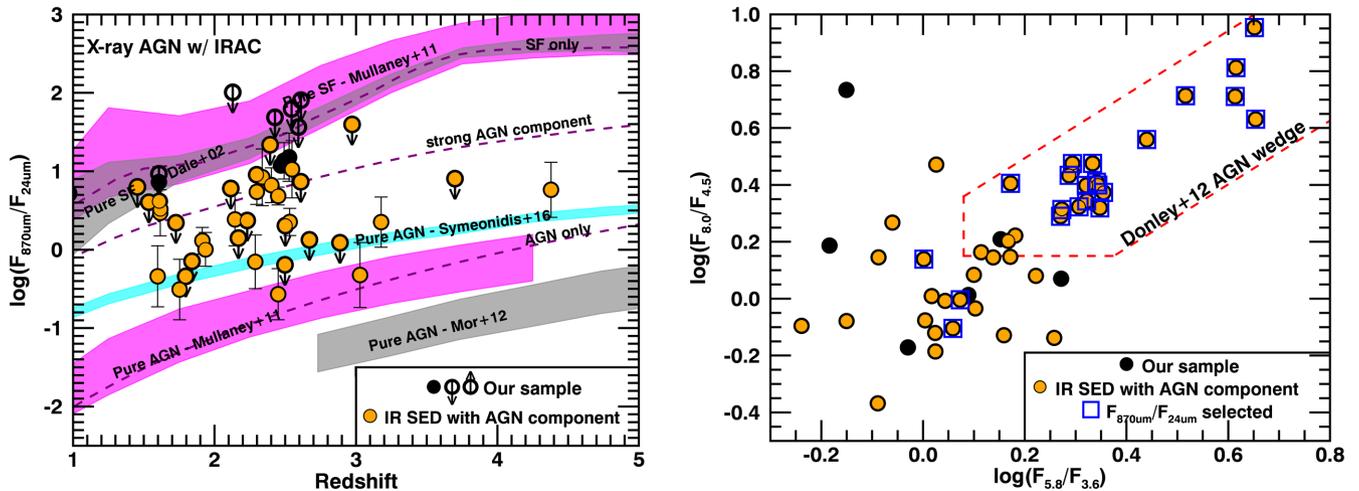
Figure 7. Comparison of the $F_{870\,\mu m}/F_{24\,\mu m}$ ratio selection to the commonly used IR colour selection for the 50 X-ray AGN that are detected in all four IRAC bands. Left: the $F_{870\,\mu m}/F_{24\,\mu m}$ ratio as a function of redshift. Using the 'strong AGN component' line (dashed purple curve) as a selection limit for AGN candidates, we find that 22/50 sources are selected. Right: the colour–colour diagram based on IRAC photometry for our sample of X-ray AGN. The AGN selection criteria of Donley et al. (2012) are shown with the dashed lines, with sources within the enclosed area being AGN. The sources that are selected as AGN candidates from the 'strong AGN component' $F_{870\,\mu m}/F_{24\,\mu m}$ line are highlighted with a blue square. We find that the majority of the $F_{870\,\mu m}/F_{24\,\mu m}$ selected AGN candidates (19/22) are also selected by their IRAC colours. In both plots, we indicate the sources where the best-fitting solution from the SED fitting requires an AGN contributing $\gtrsim 20\%$ with yellow centres. The sources with weaker AGN components (contributing ≈ 20–50% of the IR luminosity), can be missed by both colour criteria.

moderate X-ray luminosities displayed by these sources (0.5–8 keV luminosities of 10^{42}–$10^{44.5}$ erg s^{-1}).

Overall, the $F_{870\,\mu m}/F_{24\,\mu m}$ selection limit based on equation (1) can successfully identify sources with strong AGN components in a variety of different samples. This demonstrates the potential of the $F_{870\,\mu m}/F_{24\,\mu m}$-redshift plane as a selection tool for AGN candidates, especially in the future where deep MIR, and sub-mm surveys will be available through observatories such as the James Webb Space Telescope (JWST) and ALMA.

6 SUMMARY AND CONCLUSIONS

We use deep 870 μm ALMA observations to place constraints on the SFRs for a sample of 109 X-ray AGN that are faint or undetected in the *Herschel* bands. Our sample covers X-ray luminosities of $10^{42} < L_{2-8\,keV} < 10^{45}$ erg s^{-1} at redshifts of $z = 1$–4.7. Of our observed sample, 40/109 sources ($\sim$37 %) were detected at 870 μm, but even though the majority are undetected the flux limit provided by ALMA is sufficiently low to still place stronger constraints on the SFR limit value than previously possible. We make use of the SED-fitting methods of Stanley et al. (2015) in combination with photometry at 8–870 μm to fit and decompose the IR SED into AGN and star-forming components.

In summary:

(i) We find that with the depths of our ALMA observations 40/109 ($\sim$37 %) of our observed sample now have a measured SFR, 20 times more sources than previously possible for this sample with 8–500 μm *Spitzer* and *Herschel* photometries. Furthermore, the majority of our sample, 73/109 ($\sim$67 per cent), now have SFR constraints that are factors of 2–10 lower than previously possible.

(ii) With the excellent constraints at 870 μm on the star-forming component of the IR SED, we are now able to place stronger constraints on the IR emission of the AGN. Indeed, we can now identify an AGN component in 54/109 ($\sim$50 %) of our ALMA observed sample, with AGN fractions down to $\sim$20 % of the total IR emission,

where without the ALMA photometry, we could identify a MIR AGN component in only one of the sources.

(iii) We explore the parameter space of the flux density ratio of $F_{870\,\mu m}/F_{24\,\mu m}$ with redshift, and find that it can clearly identify the presence of MIR emission from the AGN, when the AGN contributes $\geq$50 % of the total IR emission. We test the $F_{870\,\mu m}/F_{24\,\mu m}$–redshift plane on two different comparison samples representing the two extremes of AGN and star formation-dominated IR emission. We suggest that this method could be developed as a tool for identifying AGN in future deep sub-mm and MIR surveys (e.g. combining ALMA and JWST data).

Overall, we have demonstrated the importance of deep ALMA sub-mm observations for constraining the moderate to low SFRs of galaxies hosting AGN. With the build-up of deep ALMA observations of large galaxy samples we will be able to use the sub-mm to MIR colours, such as the $F_{870\,\mu m}/F_{24\,\mu m}$ ratio to identify the presence of AGN emission in the IR.

REFERENCES

Aird J., Coil A. L., Georgakakis A., Nandra K., Barro G., Pérez-González P. G., 2015, MNRAS, 451, 1892

Alexander D. M., Hickox R. C., 2012, NAR, 56, 93

Alexander D. M., Bauer F. E., Chapman S. C., Smail I., Blain A. W., Brandt W. N., Ivison R. J., 2005, ApJ, 632, 736

Azadi M. et al., 2015, ApJ, 806, 187

Blain A. W., Smail I., Ivison R. J., Kneib J.-P., Frayer D. T., 2002, Phys. Rep., 369, 111

Bonfield D. G. et al., 2011, MNRAS, 416, 13

Bower R. G., Benson A. J., Malbon R., Helly J. C., Frenk C. S., Baugh C. M., Cole S., Lacey C. G., 2006, MNRAS, 370, 645

Bridge C. R. et al., 2013, ApJ, 769, 91

Casey C. M. et al., 2013, MNRAS, 436, 1919

Chabrier G., 2003, PASP, 115, 763

Chen C.-T. J. et al., 2013, ApJ, 773, 3

Civano F. et al., 2012, ApJS, 201, 30

Coppin K. et al., 2010, ApJ, 713, 503

Dale D. A., Helou G., 2002, ApJ, 576, 159

Damen M. et al., 2011, ApJ, 727, 1

Danielson A. L. R. et al., 2017, ApJ, 840, 78

Del Moro A. et al., 2013, A&A, 549, A59

Delvecchio I. et al., 2014, MNRAS, 439, 2736

Donley J. L. et al., 2012, ApJ, 748, 142

Eisenhardt P. R. M. et al., 2012, ApJ, 755, 173

Elbaz D. et al., 2011, A&A, 533, A119

Elvis M. et al., 2009, ApJS, 184, 158

Fabian A. C., 2012, ARA&A, 50, 455

Gabor J. M., Bournaud F., 2013, MNRAS, 434, 606

Genel S. et al., 2014, MNRAS, 445, 175

Gürkan G. et al., 2015, MNRAS, 452, 3776

Harris K. et al., 2016, MNRAS, 457, 4179

Harrison C. M., 2017, Nat. Astron., 1, 0165

Harrison C. M. et al., 2012, ApJ, 760, L15

Harrison C. M. et al., 2016, MNRAS, 457, L122

Hickox R. C., Mullaney J. R., Alexander D. M., Chen C.-T. J., Civano F. M., Goulding A. D., Hainline K. N., 2014, ApJ, 782, 9

Hodge J. A. et al., 2013, ApJ, 768, 91

Hsu L.-T. et al., 2014, ApJ, 796, 60

Jones S. F. et al., 2014, MNRAS, 443, 146

Jones S. F. et al., 2015, MNRAS, 448, 3325

Kalfountzou E. et al., 2014, MNRAS, 442, 1181

Karim A. et al., 2013, MNRAS, 432, 2

Laird E. S., Nandra K., Pope A., Scott D., 2010, MNRAS, 401, 2763

Lani C., Netzer H., Lutz D., 2017, MNRAS, 471, 59

Lanzuisi G. et al., 2017, A&A, 602, A123

Leipski C. et al., 2013, ApJ, 772, 103

Lonsdale C. J. et al., 2015, ApJ, 813, 45

Luo B. et al., 2017, ApJS, 228, 2

Lutz D., Maiolino R., Spoon H. W. W., Moorwood A. F. M., 2004, A&A, 418, 465

Lutz D. et al., 2010, ApJ, 712, 1287

Lutz D. et al., 2011, A&A, 532, A90

Lyu J., Rieke G. H., 2017, ApJ, 841, 76

Magnelli B. et al., 2013, A&A, 553, A132

Marchesi S. et al., 2016, ApJ, 817, 34

McAlpine S., Bower R. G., Harrison C. M., Crain R. A., Schaller M., Schaye J., Theuns T., 2017, MNRAS, 468, 3395

Mor R., Netzer H., 2012, MNRAS, 420, 526

Mullaney J. R., Alexander D. M., Goulding A. D., Hickox R. C., 2011, MNRAS, 414, 1082

Mullaney J. R. et al., 2012a, ApJ, 753, L30

Mullaney J. R. et al., 2012b, MNRAS, 419, 95

Mullaney J. R. et al., 2015, MNRAS, 453, L83

Netzer H., Lani C., Nordon R., Trakhtenbrot B., Lira P., Shemmer O., 2016, ApJ, 819, 123

Oliver S. J. et al., 2012, MNRAS, 424, 1614

Page M. J. et al., 2012, Nature, 485, 213

Pope A. et al., 2008, ApJ, 675, 1171

Rafferty D. A., Brandt W. N., Alexander D. M., Xue Y. Q., Bauer F. E., Lehmer B. D., Luo B., Papovich C., 2011, ApJ, 742, 3

Rosario D. J. et al., 2012, A&A, 545, A45

Rosario D. J. et al., 2013, A&A, 560, A72

Sanders D. B. et al., 2007, ApJS, 172, 86

Schaye J. et al., 2015, MNRAS, 446, 521

Scholtz J. et al., 2018, MNRAS, 475, 1288

Schreiber C. et al., 2015, A&A, 575, A74

Schwarz G., 1978, Ann. Stat., 6, 461

Shao L. et al., 2010, A&A, 518, L26

Silva L., Granato G. L., Bressan A., Danese L., 1998, ApJ, 509, 103

Simpson J. M. et al., 2014, ApJ, 788, 125

Simpson J. M. et al., 2015, ApJ, 807, 128

Stanley F., Harrison C. M., Alexander D. M., Swinbank A. M., Aird J. A., Del Moro A., Hickox R. C., Mullaney J. R., 2015, MNRAS, 453, 591

Stanley F. et al., 2017, MNRAS, 472, 2221

Stern D. et al., 2005, ApJ, 631, 163

Swinbank A. M. et al., 2014, MNRAS, 438, 1267

Symeonidis M., Giblin B. M., Page M. J., Pearson C., Bendo G., Seymour N., Oliver S. J., 2016, MNRAS, 459, 257

Teplitz H. I. et al., 2011, AJ, 141, 1

Tsai C.-W. et al., 2015, ApJ, 805, 90

Valiante E., Lutz D., Sturm E., Genzel R., Tacconi L. J., Lehnert M. D., Baker A. J., 2007, ApJ, 660, 1060

Volonteri M., Capelo P. R., Netzer H., Bellovary J., Dotti M., Governato F., 2015, MNRAS, 449, 1470

Wang S. X. et al., 2013, ApJ, 778, 179

Wardlow J. L. et al., 2011, MNRAS, 415, 1479

Xue Y. Q. et al., 2011, ApJS, 195, 10

Yang G. et al., 2017, ApJ, 842, 72

SUPPORTING INFORMATION

Supplementary data are available at *MNRAS* online.

Figure A1. The best-fitting SEDs for all sources in our X-ray AGN sample.

Figure A2. The best-fitting SEDs for all sources of the MIR-bright AGN comparison sample at redshifts of $1 < z < 5$.

Figure A3. The best-fitting SEDs for all sources of the A-LESS SMG comparison sample at redshifts of $1 < z < 5$.

Please note: Oxford University Press is not responsible for the content or functionality of any supporting materials supplied by the authors. Any queries (other than missing material) should be directed to the corresponding author for the article.

APPENDIX A: SOURCE TABLES AND SED FITS FOR OUR X-RAY AGN SAMPLE AND THE TWO COMPARISON SAMPLES

In this appendix, we present the best-fitting SEDs and tabulated results, for our sample of X-ray AGN, and the two comparison samples of *WISE* AGN-dominated sources and star-forming galaxies from the A-LESS survey (see Section 2.4 for details). Tables A1 and A2 contain the source properties and best-fitting SED results of our sample of X-ray AGN split into the two deep field of GOODS-S and C-COSMOS, while Tables A3 and A4 contain the properties and best-fitting SED results of the two comparison samples. Fig. A1 contains the best-fitting SEDs of our X-ray AGN sample, Fig. A2 the best-fitting SEDs of the *WISE* AGN-dominated sample, and Fig. A3 the best-fitting SEDs of the star-forming galaxy sample.

Table A1. Properties of the ALMA observed X-ray sample in the GOODS-S field.

Field	XID[a]	z[b]	$L_{2-8\,\mathrm{keV}}$[c] (erg s^{-1})	$L_{\mathrm{IR,\,SF}}$[d] ($\times 10^{45}$ erg s^{-1})	$L_{\mathrm{IR,\,AGN}}$[e] ($\times 10^{45}$ erg s^{-1})	AGN flag[f]
GS	509	1.101	1.36×10^{42}	<0.66	<0.1	-1
GS	195	1.452	1.48×10^{43}	$1.09^{+0.50}_{-0.69}$	$-$	0
GS	167	1.455	2.12×10^{43}	<1.06	$0.61^{+0.09}_{-0.09}$	2
GS	276	1.519	2.22×10^{42}	$1.38^{+0.00}_{-0.00}$	$-$	0
GS	257	1.536	0.85×10^{44}	<2.06	$0.72^{+0.16}_{-0.16}$	2
GS	211	1.601	2.76×10^{43}	<1.24	<0.32	-1
GS	184	1.605	3.11×10^{42}	<1.81	<0.32	-1
GS	163	1.607	2.54×10^{42}	<2.04	<0.51	-1
GS	318	1.607	0.85×10^{42}	$1.64^{+0.16}_{-0.16}$	$-$	0
GS	405	1.609	0.81×10^{43}	<1.08	$0.65^{+0.11}_{-0.11}$	2
GS	503	1.609	0.32×10^{43}	<2.06	<0.32	-1
GS	88	1.616	0.55×10^{44}	$2.10^{+0.23}_{-0.23}$	$0.90^{+0.22}_{-0.22}$	2
GS	344	1.617	0.42×10^{44}	$8.49^{+0.24}_{-0.24}$	$2.28^{+0.36}_{-0.36}$	2
GS	308	1.727	0.72×10^{44}	<0.93	$1.01^{+0.15}_{-0.15}$	2
GS	221	1.887	0.50×10^{43}	<1.96	<0.52	-1
GS	463	1.910	0.95×10^{42}	<2.27	<0.54	-1
GS	155	2.019	2.05×10^{42}	<2.09	<0.64	-1
GS	158	2.046	1.03×10^{43}	<2.78	<0.66	-1
GS	522	2.115	0.36×10^{44}	<2.56	$1.46^{+0.31}_{-0.31}$	2
GS	388	2.129	0.88×10^{43}	<3.03	<0.44	-1
GS	320	2.145	1.18×10^{43}	$2.70^{+0.63}_{-0.47}$	$3.7^{+0.4}_{-0.6}$	2
GS	277	2.209	0.50×10^{44}	<1.97	<0.83	-1
GS	326	2.298	1.68×10^{43}	<1.73	$0.73^{+0.26}_{-0.26}$	2
GS	633	2.299	0.49×10^{44}	$2.28^{+1.22}_{-1.36}$	$1.99^{+0.77}_{-0.75}$	2
GS	123	2.331	1.01×10^{43}	<2.09	<0.98	-1
GS	185	2.337	1.58×10^{42}	$0.89^{+0.50}_{-0.57}$	$0.42^{+0.31}_{-0.28}$	2
GS	310	2.392	2.65×10^{43}	$4.40^{+0.37}_{-0.37}$	$-$	0
GS	444	2.393	0.50×10^{44}	<2.75	0.75×10^{45}	2
GS	215	2.402	2.50×10^{43}	$1.93^{+1.06}_{-1.23}$	$1.43^{+0.67}_{-0.62}$	2
GS	677	2.414	0.45×10^{44}	<4.72	<1.09	-1
GS	199	2.417	2.33×10^{43}	<4.70	<1.09	-1
GS	305	2.419	0.93×10^{43}	<2.16	<1.09	-1
GS	574	2.427	0.87×10^{43}	<4.23	<0.97	-1
GS	301	2.469	0.35×10^{44}	$7.51^{+0.28}_{-0.28}$	$-$	0
GS	422	2.492	0.50×10^{43}	$2.98^{+0.71}_{-2.09}$	$-$	0
GS	410	2.527	0.40×10^{44}	$2.78^{+0.75}_{-1.95}$	$-$	0
GS	351	2.532	2.50×10^{44}	$1.37^{+0.24}_{-0.24}$	$7.38^{+0.75}_{-0.75}$	2
GS	290	2.545	0.83×10^{44}	<6.56	<1.55	-1
GS	93	2.573	0.69×10^{44}	<6.29	<1.32	-1
GS	593	2.593	0.53×10^{44}	<6.44	<1.54	-1
GS	137	2.610	1.66×10^{44}	<3.21	$4.77^{+0.56}_{-0.56}$	2
GS	294	2.611	0.39×10^{44}	<5.46	<0.96	-1
GS	359	2.728	0.50×10^{44}	<6.56	<1.57	-1
GS	466	2.775	2.99×10^{43}	<6.35	$2.28^{+0.68}_{-0.68}$	2
GS	254	2.801	2.49×10^{43}	<6.01	<1.70	-1
GS	528	2.973	0.56×10^{44}	<8.68	$2.04^{+0.65}_{-0.65}$	2
GS	456	3.173	2.65×10^{43}	<1.93	<2.47	-1
GS	371	3.242	0.63×10^{44}	$7.60^{+3.60}_{-4.43}$	$-$	0
GS	386	3.256	0.94×10^{43}	$1.58^{+0.97}_{-1.15}$	$-$	0
GS	129	3.446	1.48×10^{44}	<1.82	$3.56^{+1.10}_{-1.10}$	2
GS	262	3.660	1.61×10^{44}	$3.25^{+0.93}_{-0.82}$	$2.35^{+0.77}_{-0.69}$	2
GS	412	3.700	2.70×10^{44}	<2.91	$7.15^{+0.93}_{-0.93}$	2
GS	230	3.985	1.32×10^{44}	$1.31^{+0.71}_{-0.88}$	$-$	0
GS	534	4.379	0.85×10^{44}	$1.58^{+0.68}_{-1.24}$	$10.57^{+2.15}_{-2.11}$	2
GS	156	4.651	0.91×10^{44}	$7.06^{+2.37}_{-3.69}$	$-$	0

[a]The X-ray ID of the source in the Xue et al. (2011) catalogue; [b]The redshift of the source from Hsu et al. (2014); [c]The X-ray HB luminosity of the source; [d]The IR luminosity due to star formation derived by the best-fitting SED solution; [e]The IR luminosity due to the AGN derived from the the best-fitting SED solution; [f]Flag for the AGN component of the fits, where -1 = only upper limit constraints, 0 = SED fit does not require an AGN component, 1 = SED fit requires an AGN component, but has a weak contribution and is uncertain (<20% of the IR luminosity), and 2 = SED fit requires an AGN component with significant contribution (≥ 20% of the IR luminosity).

Table A2. Properties of the ALMA observed X-ray sample in the COMSOS field.

Field	XID[a]	z[b]	$L_{2-8\,\mathrm{keV}}$[c] (erg s^{-1})	$L_{\mathrm{IR,\,SF}}$[d] ($\times\,10^{45}$ erg s^{-1})	$L_{\mathrm{IR,\,AGN}}$[e] ($\times\,10^{45}$ erg s^{-1})	AGN flag[f]
C	85	1.349	0.89×10^{44}	<1.10	<0.19	-1
C	434	1.530	0.51×10^{45}	$0.79^{+0.52}_{-0.53}$	$1.84^{+0.47}_{-0.47}$	2
C	1214	1.594	1.41×10^{44}	$0.88^{+0.63}_{-0.65}$	$-$	0
C	87	1.598	1.01×10^{45}	$0.63^{+0.50}_{-0.50}$	$3.39^{+0.60}_{-0.60}$	2
C	581	1.708	0.39×10^{45}	<1.08	<0.39	-1
C	330	1.753	0.57×10^{45}	$0.61^{+0.38}_{-0.41}$	$5.33^{+1.25}_{-1.25}$	2
C	53	1.787	2.22×10^{44}	<1.69	<0.44	-1
C	474	1.796	0.41×10^{45}	<1.15	$5.21^{+0.95}_{-0.95}$	2
C	532	1.796	0.38×10^{45}	<1.11	$2.50^{+0.60}_{-0.60}$	2
C	86	1.831	2.87×10^{44}	$0.59^{+0.45}_{-0.47}$	$-$	0
C	915	1.841	1.37×10^{44}	<1.19	$4.37^{+1.04}_{-1.00}$	2
C	987	1.860	1.33×10^{44}	<1.68	$0.67^{+0.25}_{-0.25}$	2
C	1144	1.912	1.61×10^{44}	$1.48^{+1.17}_{-0.96}$	$-$	0
C	62	1.914	0.40×10^{45}	$1.37^{+0.84}_{-0.90}$	$0.34^{+0.09}_{-0.09} \times 10^{46}$	2
C	90	1.932	0.38×10^{45}	<1.25	$1.36^{+0.42}_{-0.42}$	2
C	954	1.936	2.32×10^{44}	$1.07^{+0.65}_{-0.70} \times 10^{45}$	$0.36^{+0.10}_{-0.09} \times 10^{46}$	2
C	81	1.991	1.55×10^{44}	$0.87^{+0.52}_{-0.57} \times 10^{45}$	$2.80^{+0.79}_{-0.78} \times 10^{45}$	2
C	351	2.018	0.57×10^{45}	<1.69	$3.36^{+0.88}_{-0.88}$	2
C	659	2.045	1.50×10^{44}	<1.16	$1.74^{+0.52}_{-0.52}$	2
C	580	2.111	0.43×10^{45}	<1.73	$0.96^{+0.38}_{-0.38}$	2
C	706	2.113	1.16×10^{44}	<1.74	<0.73	-1
C	960	2.122	1.06×10^{44}	$1.31^{+0.76}_{-0.85}$	$2.15^{+0.74}_{-0.72}$	2
C	914	2.146	1.57×10^{44}	$1.36^{+0.79}_{-0.89}$	$0.65^{+0.50}_{-0.47}$	2
C	1620	2.169	0.53×10^{45}	<1.66	$3.77^{+0.97}_{-0.97}$	2
C	1085	2.231	0.52×10^{45}	<1.82	$2.69^{+0.76}_{-0.76}$	2
C	1205	2.255	1.22×10^{44}	$0.96^{+0.68}_{-0.74}$	$-$	0
C	467	2.288	0.94×10^{45}	$1.05^{+0.59}_{-0.68}$	$8.51^{+2.02}_{-2.01}$	2
C	1127	2.390	1.99×10^{44}	<2.70	$1.29^{+0.49}_{-0.49}$	2
C	451	2.450	0.65×10^{45}	$0.67^{+0.56}_{-0.60}$	$27.34^{+3.86}_{-3.86}$	2
C	1215	2.450	1.85×10^{44}	$6.37^{+0.64}_{-2.67}$	$5.72^{+1.28}_{-1.77}$	2
C	1143	2.454	1.54×10^{44}	<1.68	<1.14	-1
C	72	2.475	0.56×10^{45}	<1.80	$4.11^{+1.25}_{-1.25}$	2
C	976	2.478	1.14×10^{44}	<1.63	<1.18	-1
C	352	2.498	0.63×10^{45}	<1.67	$12.73^{+2.92}_{-2.92}$	2
C	970	2.501	0.64×10^{45}	<2.55	$6.16^{+1.73}_{-1.73}$	2
C	708	2.548	1.42×10^{44}	$1.93^{+1.03}_{-1.22}$	$1.00^{+0.68}_{-0.63}$	2
C	31	2.611	0.90×10^{45}	$1.77^{+0.93}_{-1.12}$	$8.1^{+3.1}_{-3.1}$	2
C	1216	2.663	1.84×10^{44}	<2.68	$4.92^{+1.89}_{-1.82}$	2
C	365	2.671	0.55×10^{45}	<2.59	$11.60^{+2.75}_{-2.75}$	2
C	121	2.791	0.43×10^{45}	<2.72	<1.68	-1
C	58	2.798	0.56×10^{45}	<2.60	<1.69	-1
C	459	2.887	0.86×10^{45}	<2.72	$19.41^{+3.28}_{-3.28}$	2
C	1246	2.888	1.75×10^{44}	<2.70	<1.86	-1
C	1219	2.946	2.23×10^{44}	<2.53	<1.98	-1
C	149	2.955	0.62×10^{45}	<2.91	$2.78^{+1.04}_{-1.04}$	2
C	529	3.017	0.61×10^{45}	<2.82	<2.12	-1
C	75	3.029	0.86×10^{45}	$0.98^{+0.83}_{-0.91}$	$27.58^{+5.07}_{-5.07}$	2
C	124	3.072	0.37×10^{45}	<2.65	<2.24	-1
C	83	3.075	0.55×10^{45}	<2.55	<2.25	-1
C	1247	3.087	1.21×10^{44}	<2.54	<2.27	-1
C	917	3.090	1.45×10^{44}	$9.24^{+4.27}_{-5.26}$	$-$	0
C	953	3.095	1.98×10^{44}	<2.72	<2.29	-1
C	558	3.100	0.95×10^{45}	<2.70	<2.30	-1
C	965	3.178	2.86×10^{44}	$1.79^{+0.83}_{-1.08}$	$11.62^{+3.00}_{-3.00}$	2

[a]The X-ray ID of the source in the Civano et al. (2012) catalogue; [b]The redshift of the source from Marchesi et al. (2016); [c]The 2–10 keV luminosity of the source; [d]The IR luminosity due to star formation derived by the best-fitting SED solution; [e]The IR luminosity due to the AGN derived from the the best-fitting SED solution; [f]Flag for the AGN component of the fits, where -1 = only upper limit constraints, 0 = SED fit does not require an AGN component, 1 = SED fit requires an AGN component, but has a weak contribution and is uncertain ($<20\%$ of the IR luminosity), and 2 = SED fit requires an AGN component with significant contribution ($\geq 20\%$ of the IR luminosity).

Table A3. SED-fitting results for the comparison sample of *WISE* AGN-dominated sources.

WISE ID[a]	z[b]	$L_{IR, SF}$[c] $(\times 10^{46} \text{ erg s}^{-1})$	$L_{IR, AGN}$[d] $(\times 10^{46} \text{ erg s}^{-1})$	AGN flag[e]
W1514−3411	1.090	<0.34	$1.72^{+0.35}_{-0.35}$	2
W0811−2225	1.110	<0.68	$2.21^{+0.48}_{-0.48}$	2
W1439−3725	1.190	<0.23	$1.41^{+0.32}_{-0.32}$	2
W0404−2436	1.260	$0.85^{+0.53}_{-0.61}$	$1.95^{+0.50}_{-0.50}$	2
W0642−2728	1.340	$0.59^{+0.44}_{-0.43}$	$1.41^{+0.39}_{-0.39}$	2
W0354−3308	1.370	<0.49	$3.40^{+0.65}_{-0.65}$	2
W0630−2120	1.440	$1.37^{+1.02}_{-1.00}$	$2.80^{+0.66}_{-0.66}$	2
W1500−0649	1.500	$2.99^{+0.13}_{-0.13}$	$9.64^{+0.39}_{-0.39}$	2
W0304−3108	1.540	$0.69^{+0.47}_{-0.48}$	$6.77^{+1.19}_{-1.19}$	2
W1541−1144	1.580	$0.26^{+0.19}_{-0.20}$	$5.78^{+1.15}_{-1.15}$	2
W1951−0420	1.580	<0.44	$5.02^{+1.00}_{-1.00}$	2
W0719−3349	1.630	$1.33^{+1.14}_{-0.86}$	$3.17^{+0.77}_{-0.80}$	2
W1308−3447	1.650	$0.29^{+0.22}_{-0.22}$	$6.61^{+1.21}_{-1.21}$	2
W1400−2919	1.670	<0.38	$9.92^{+1.72}_{-1.72}$	2
W0525−3614	1.690	<0.63	$3.11^{+0.68}_{-0.68}$	2
W0549−3739	1.710	$0.55^{+0.38}_{-0.39}$	$2.44^{+0.60}_{-0.60}$	2
W0823−0624	1.750	<0.76	$9.44^{+1.72}_{-1.72}$	2
W0536−2703	1.790	$0.70^{+0.46}_{-0.48}$	$5.97^{+1.27}_{-1.27}$	2
W1703−0517	1.800	$0.18^{+0.14}_{-0.15}$	$7.14^{+1.63}_{-1.63}$	2
W1958−0746	1.800	<0.39	$7.79^{+1.56}_{-1.56}$	2
W1412−2020	1.820	$0.62^{+0.44}_{-0.46}$	$7.74^{+1.50}_{-1.50}$	2
W1641−0548	1.840	$0.57^{+0.37}_{-0.39}$	$7.06^{+1.48}_{-1.48}$	2
W1434−0235	1.920	<0.38	$6.19^{+1.24}_{-1.24}$	2
W0526−3225	1.980	$5.04^{+3.10}_{-3.33}$	$24.28^{+4.25}_{-4.24}$	2
W0614−0936	2.000	<0.77	$7.52^{+1.55}_{-1.55}$	2
W1657−1740	2.000	<0.33	$10.07^{+2.11}_{-2.11}$	2
W1707−0939	2.000	<0.43	$6.39^{+1.89}_{-1.89}$	2
W2040−3904	2.000	$2.30^{+0.22}_{-1.83}$	$6.68^{+1.56}_{-1.61}$	2
W1653−0102	2.020	<0.33	$8.04^{+1.69}_{-1.69}$	2
W0519−0813	2.050	<0.64	$6.76^{+1.45}_{-1.45}$	2
W1634−1721	2.080	<0.36	$6.05^{+1.55}_{-1.55}$	2
W0613−3407	2.180	<0.77	$11.79^{+2.18}_{-2.18}$	2
W1513−2210	2.200	$1.25^{+0.74}_{-0.82}$	$12.38^{+2.55}_{-2.55}$	2
W1936−3354	2.240	$0.38^{+0.25}_{-0.28}$	$9.87^{+2.15}_{-2.15}$	2
W2000−2802	2.280	<0.41	$13.97^{+2.99}_{-2.99}$	2
W2059−3541	2.380	<0.42	$4.26^{+0.79}_{-0.79}$	2
W2021−2611	2.440	$1.25^{+0.71}_{-0.81}$	$6.69^{+1.85}_{-1.85}$	2
W1343−1136	2.490	$0.54^{+0.32}_{-0.36}$	$9.15^{+2.11}_{-2.11}$	2
W1521+0017	2.630	−	$22.12^{+3.26}_{-3.26}$	2
W0439−3159	2.820	$1.69^{+0.89}_{-1.07}$	$10.22^{+2.37}_{-2.37}$	2
W1702−0811	2.850	<0.43	$25.91^{+6.85}_{-6.85}$	2

[a]The *WISE* ID of the source as given in Lonsdale et al. (2015); [b]The redshift of the source from Lonsdale et al. (2015); [c]The IR luminosity due to star formation derived by the best-fitting SED solution; [d]The IR luminosity due to the AGN derived from the the best-fitting SED solution; [e]Flag for the AGN component of the fits, where −1 = only upper limit constraints, 0 = SED fit does not require an AGN component, 1 = SED fit requires an AGN component, but has a weak contribution and is uncertain (<20% of the IR luminosity), and 2 = SED fit requires an AGN component with significant contribution (≥20% of the IR luminosity).

Table A4. SED-fitting results for the comparison sample of star formation galaxies.

A-LESS ID[a]	z[b]	$L_{\text{IR, SF}}$[c] ($\times 10^{46}$ erg s^{-1})	$L_{\text{IR, AGN}}$[d] ($\times 10^{45}$ erg s^{-1})	AGN flag[e]
A-LESS 103.2	1.000	$0.63^{+0.08}_{-0.60}$	–	0
A-LESS 089.1	1.170	$0.41^{+0.07}_{-0.34}$	$0.12^{+0.03}_{-0.12}$	1
A-LESS 088.1	1.268	$0.55^{+0.32}_{-0.38}$	–	0
A-LESS 062.2	1.361	$1.06^{+0.05}_{-0.84}$	–	0
A-LESS 051.1	1.363	$0.21^{+0.23}_{-0.02}$	–	0
A-LESS 080.2	1.365	$0.34^{+0.04}_{-0.18}$	–	0
A-LESS 098.1	1.373	$0.91^{+0.06}_{-0.67}$	–	0
A-LESS 055.1	1.378	$0.17^{+0.09}_{-0.00}$	–	0
A-LESS 003.2	1.390	$0.16^{+0.18}_{-0.03}$	–	0
A-LESS 029.1	1.439	$1.61^{+0.11}_{-1.40}$	–	0
A-LESS 049.2	1.465	$0.44^{+0.05}_{-0.28}$	–	0
A-LESS 084.2	1.471	$0.49^{+0.11}_{-0.32}$	$0.08^{+0.40}_{-0.16}$	1
A-LESS 063.1	1.490	$0.73^{+0.00}_{-0.49}$	–	0
A-LESS 017.1	1.540	$0.95^{+0.05}_{-0.62}$	–	0
A-LESS 114.2	1.606	$0.97^{+0.07}_{-0.75}$	$0.32^{+0.14}_{-0.35}$	1
A-LESS 043.1	1.705	$0.38^{+0.45}_{-0.12}$	–	0
A-LESS 079.2	1.769	$0.81^{+0.19}_{-0.56}$	$1.90^{+2.37}_{-2.02}$	2
A-LESS 074.1	1.800	$0.86^{+0.80}_{-0.58}$	–	0
A-LESS 126.1	1.815	$0.54^{+0.08}_{-0.30}$	–	0
A-LESS 092.2	1.900	$0.28^{+0.11}_{-0.14}$	–	0
A-LESS 015.1	1.925	$1.72^{+1.21}_{-1.06}$	–	0
A-LESS 043.3	1.975	$0.29^{+0.22}_{-0.13}$	–	0
A-LESS 122.1	2.025	$2.19^{+0.15}_{-1.75}$	$9.24^{+17.91}_{-2.42}$	2
A-LESS 079.1	2.045	$1.50^{+0.00}_{-0.00}$	–	0
A-LESS 059.2	2.090	$0.93^{+0.14}_{-0.71}$	–	0
A-LESS 070.1	2.093	$2.58^{+0.19}_{-1.99}$	$4.12^{+1.07}_{-4.25}$	1
A-LESS 082.1	2.095	$2.06^{+0.00}_{-0.00}$	–	0
A-LESS 075.4	2.100	$2.88^{+2.68}_{-1.43}$	–	0
A-LESS 107.3	2.115	$2.96^{+3.30}_{-1.90}$	–	0
A-LESS 067.1	2.135	$1.49^{+0.40}_{-0.94}$	–	0
A-LESS 081.1	2.145	$2.40^{+0.21}_{-1.81}$	$3.99^{+3.79}_{-4.18}$	1
A-LESS 019.2	2.170	$0.34^{+0.50}_{-0.25}$	–	0
A-LESS 002.1	2.191	$1.68^{+0.13}_{-0.13}$	–	0
A-LESS 022.1	2.266	$2.26^{+0.21}_{-1.73}$	$6.17^{+1.45}_{-5.93}$	2
A-LESS 088.5	2.291	$1.57^{+0.16}_{-1.21}$	$1.60^{+0.47}_{-1.67}$	1
A-LESS 075.2	2.294	$0.56^{+0.20}_{-0.18}$	–	0
A-LESS 102.1	2.296	$0.82^{+0.43}_{-0.44}$	–	0
A-LESS 112.1	2.314	$1.78^{+1.26}_{-1.12}$	–	0
A-LESS 087.1	2.318	$0.80^{+0.15}_{-0.65}$	$8.20^{+1.68}_{-2.48}$	2
A-LESS 006.1	2.330	$1.30^{+0.93}_{-0.89}$	–	0
A-LESS 045.1	2.340	$2.24^{+0.17}_{-1.98}$	–	0
A-LESS 055.5	2.345	$0.35^{+0.25}_{-0.23}$	–	0
A-LESS 093.1	2.350	$0.89^{+0.76}_{-0.52}$	–	0
A-LESS 083.1	2.360	$1.80^{+0.21}_{-0.21}$	–	0
A-LESS 062.1	2.380	$0.87^{+0.95}_{-0.60}$	–	0
A-LESS 019.1	2.410	$2.32^{+0.17}_{-2.03}$	–	0
A-LESS 118.1	2.413	$1.53^{+0.19}_{-1.24}$	–	0
A-LESS 039.1	2.440	$1.13^{+0.71}_{-0.68}$	–	0
A-LESS 017.2	2.441	$0.55^{+0.22}_{-0.22}$	–	0
A-LESS 037.2	2.463	$0.42^{+0.31}_{-0.29}$	–	0
A-LESS 038.1	2.470	$1.60^{+0.17}_{-0.99}$	–	0
A-LESS 034.1	2.510	$1.01^{+0.89}_{-0.59}$	–	0
A-LESS 110.1	2.545	$1.50^{+0.00}_{-1.05}$	–	0
A-LESS 041.1	2.546	$1.90^{+0.38}_{-1.25}$	–	0
A-LESS 066.1	2.554	$1.24^{+0.18}_{-0.96}$	$12.33^{+3.15}_{-2.92}$	2
A-LESS 075.1	2.556	$1.09^{+0.50}_{-0.72}$	$17.40^{+4.98}_{-5.82}$	2
A-LESS 088.1	2.565	$1.40^{+0.18}_{-0.99}$	–	0
A-LESS 017.3	2.575	$0.76^{+0.08}_{-0.11}$	–	0
A-LESS 020.1	2.575	$1.42^{+0.27}_{-0.79}$	–	0

Table A4. – *continued*

A-LESS ID[a]	z[b]	$L_{\rm IR, SF}$[c] $(\times 10^{46}\ \rm erg\,s^{-1})$	$L_{\rm IR, AGN}$[d] $(\times 10^{45}\ \rm erg\,s^{-1})$	AGN flag[e]
A-LESS 011.1	2.680	$1.93^{+1.17}_{-1.14}$	–	0
A-LESS 018.1	2.689	$2.56^{+0.21}_{-1.99}$	$4.83^{+2.88}_{-4.66}$	1
A-LESS 007.1	2.693	$2.67^{+0.23}_{-1.95}$	$6.30^{+5.92}_{-2.53}$	2
A-LESS 071.3	2.725	$0.36^{+0.25}_{-0.24}$	–	0
A-LESS 049.1	2.760	$2.34^{+0.19}_{-1.60}$	–	0
A-LESS 101.1	2.800	$1.54^{+0.22}_{-1.26}$	–	0
A-LESS 001.3	2.845	$1.09^{+0.18}_{-0.86}$	–	0
A-LESS 005.1	2.860	$2.87^{+0.24}_{-0.24}$	–	0
A-LESS 094.1	2.870	$1.18^{+0.24}_{-0.78}$	$2.72^{+2.39}_{-1.13}$	1
A-LESS 025.1	2.880	$3.23^{+0.19}_{-2.46}$	$4.60^{+1.05}_{-4.58}$	1
A-LESS 031.1	2.885	$3.44^{+0.16}_{-0.16}$	–	0
A-LESS 023.7	2.900	$0.46^{+0.31}_{-0.31}$	–	0
A-LESS 057.1	2.938	$1.85^{+0.24}_{-1.39}$	$9.11^{+1.93}_{-3.18}$	2
A-LESS 114.1	3.000	$1.91^{+0.27}_{-1.46}$	–	0
A-LESS 107.1	3.048	$1.05^{+0.17}_{-0.81}$	–	0
A-LESS 001.2	3.086	$0.91^{+0.42}_{-0.53}$	–	0
A-LESS 041.3	3.100	$0.72^{+0.47}_{-0.47}$	–	0
A-LESS 013.1	3.250	$2.04^{+0.58}_{-0.99}$	–	0
A-LESS 035.1	3.300	$2.20^{+0.15}_{-1.63}$	–	0
A-LESS 030.1	3.360	$1.29^{+0.75}_{-0.78}$	–	0
A-LESS 081.2	3.370	$0.64^{+0.39}_{-0.40}$	–	0
A-LESS 076.1	3.390	$1.28^{+0.53}_{-0.51}$	–	0
A-LESS 001.1	3.435	$1.56^{+0.57}_{-0.76}$	–	0
A-LESS 015.3	3.441	$0.53^{+0.32}_{-0.34}$	–	0
A-LESS 119.1	3.500	$1.48^{+0.33}_{-0.48}$	–	0
A-LESS 037.1	3.530	$1.52^{+0.18}_{-1.14}$	$15.62^{+3.07}_{-3.09}$	2
A-LESS 116.1	3.540	$1.68^{+0.20}_{-1.26}$	–	0
A-LESS 023.2	3.555	$1.45^{+0.79}_{-0.84}$	–	0
A-LESS 072.1	3.596	$1.36^{+0.71}_{-0.76}$	–	0
A-LESS 035.2	3.700	$0.39^{+0.23}_{-0.24}$	–	0
A-LESS 110.5	3.700	$0.66^{+0.38}_{-0.41}$	–	0
A-LESS 071.1	3.701	$1.89^{+0.27}_{-1.59}$	$89.63^{+8.92}_{-6.42}$	2
A-LESS 115.0	3.789	$3.36^{+0.19}_{-2.39}$	–	0
A-LESS 067.2	3.881	$0.90^{+0.19}_{-0.68}$	–	0
A-LESS 002.2	3.920	$2.25^{+0.27}_{-1.61}$	–	0
A-LESS 084.1	3.965	$2.00^{+0.27}_{-1.55}$	$20.26^{+3.70}_{-3.28}$	2
A-LESS 087.3	4.000	$0.70^{+0.38}_{-0.41}$	–	0
A-LESS 116.2	4.015	$1.89^{+0.24}_{-1.37}$	–	0
A-LESS 055.2	4.200	$0.69^{+0.36}_{-0.40}$	–	0
A-LESS 069.1	4.211	$1.42^{+0.63}_{-0.73}$	$7.52^{+1.94}_{-1.83}$	2
A-LESS 003.1	4.237	$4.00^{+0.18}_{-2.73}$	–	0
A-LESS 103.3	4.400	$0.43^{+0.22}_{-0.25}$	–	0
A-LESS 061.1	4.440	$2.05^{+0.23}_{-1.39}$	–	0
A-LESS 065.1	4.444	$1.25^{+0.54}_{-0.64}$	–	0
A-LESS 014.1	4.465	$3.75^{+0.24}_{-2.55}$	$7.45^{+1.62}_{-3.03}$	1
A-LESS 009.1	4.500	$4.21^{+0.22}_{-2.79}$	–	0
A-LESS 079.4	4.600	$0.55^{+0.28}_{-0.32}$	–	0
A-LESS 080.1	4.660	$1.24^{+0.57}_{-0.66}$	–	0
A-LESS 069.2	4.750	$0.73^{+0.34}_{-0.40}$	–	0
A-LESS 073.1	4.755	$1.77^{+0.75}_{-0.79}$	–	0
A-LESS 069.3	4.800	$0.64^{+0.31}_{-0.36}$	–	0
A-LESS 023.1	4.990	$3.29^{+0.17}_{-2.08}$	–	0
A-LESS 099.1	5.000	$0.66^{+0.28}_{-0.33}$	–	0

[a]The A-LESS ID of the source as given in Hodge et al. (2013); [b]The redshift of the source from Simpson et al. (2014) and Danielson et al. (2017); [c]The IR luminosity due to star formation derived by the best-fitting SED solution; [d]The IR luminosity due to the AGN derived from the the best-fitting SED solution; [e]Flag for the AGN component of the fits, where -1 = only upper limit constraints, 0 = SED fit does not require an AGN component, 1 = SED fit requires an AGN component, but has a weak contribution and is uncertain (<20 per cent of the IR luminosity), and 2 = SED fit requires an AGN component with significant contribution (≥ 20 per cent of the IR luminosity).
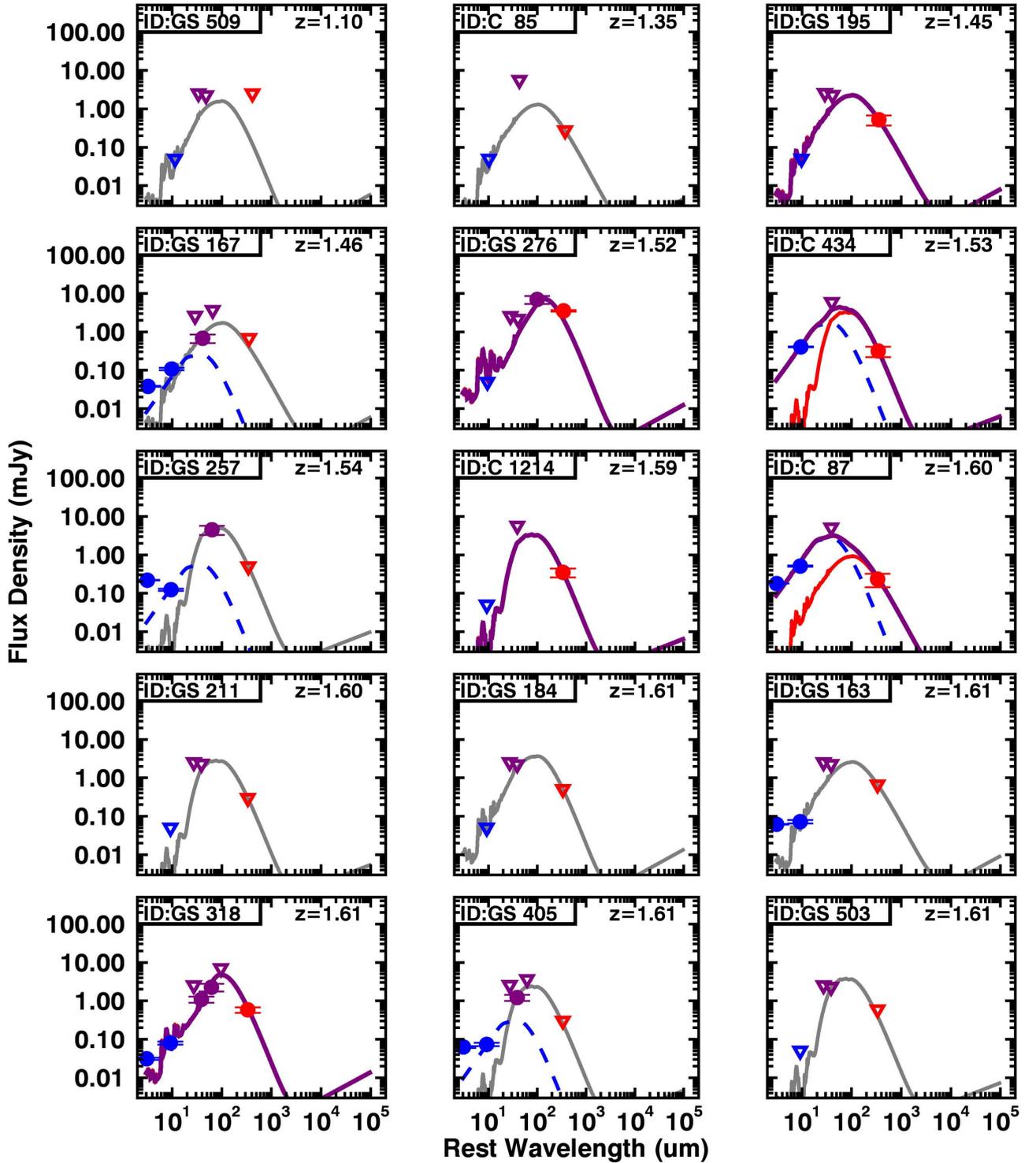
Figure A1. The best-fitting SEDs for all sources in our X-ray AGN sample. Here, we give the first 15 sources, the rest being available on the online version. The blue dashed curve is the AGN component, while the red solid curve is the star-forming component. The total combined SED is shown as a purple solid curve. The grey curves correspond to an upper limit constraint on the SF component. The photometry is colour-coded, with blue corresponding to *Spitzer*, purple to *Herschel* bands, and red to the ALMA photometry. Filled circles correspond to photometric measurements, while the inverted triangles correspond to photometric upper limits. We note that here we plot all AGN components found in our SED-fitting analysis, including weak/uncertain ones (see flag = 1 in Tables A1 and A2) that where not included in our analysis.

Figure A2. The best-fitting SEDs for all sources of the MIR-bright AGN comparison sample at redshifts of $1 < z < 5$. Here, we give the first 15 sources, the rest being available on the online version. The blue dashed curve is the AGN component, while the red solid curve is the star-forming component. The total combined SED is shown as a purple solid curve. The grey curves correspond to an upper limit constraint on the SF component. The photometry is colour-coded, with blue corresponding to *Spitzer*, purple to *Herschel* bands, and red to the ALMA photometry. Filled circles correspond to photometric measurements, while the inverted triangles correspond to photometric upper limits.

Figure A3. The best-fitting SEDs for all sources of the A-LESS SMG comparison sample at redshifts of $1 < z < 5$. Here, we give the first 15 sources, the rest being available on the online version. The blue dashed curve is the AGN component, while the red solid curve is the star-forming component. The total combined SED is shown as a purple solid curve. The grey curves correspond to an upper limit constraint on the SF component. The photometry is colour-coded, with blue corresponding to *Spitzer*, purple to *Herschel* bands, and red to the ALMA photometry. Filled circles correspond to photometric measurements, while the inverted triangles correspond to photometric upper limits. We note that here we plot all AGN components found in our SED-fitting analysis, including weak/uncertain ones (see flag = 1 in Table A4) that where not included in our analysis.

This paper has been typeset from a TEX/LATEX file prepared by the author.